Brain Structure and Function (2019) 224:2121–2142
https://doi.org/10.1007/s00429-019-01897-7

ORIGINAL ARTICLE

Merlin modulates process outgrowth and synaptogenesis in the cerebellum

A. Toledo[1] · F. Lang[1] · M. Doengi[2] · H. Morrison[3] · V. Stein[2] · S. L. Baader[1]

Received: 25 August 2018 / Accepted: 29 May 2019 / Published online: 4 June 2019

Abstract

Neurofibromatosis type 2 (NF2) patients are prone to develop glial-derived tumors in the peripheral and central nervous system (CNS). The *Nf2* gene product –Merlin is not only expressed in glia, but also in neurons of the CNS, where its function still remains elusive. Here, we show that cerebellar Purkinje cells (PCs) of isoform-specific Merlin-deficient mice were innervated by smaller vGluT2-positive clusters at presynaptic terminals than those of wild-type mice. This was paralleled by a reduction in frequency and amplitude of miniature excitatory postsynaptic currents (mEPSC). On the contrary, in conditional transgenic mice in which Merlin expression was specifically ablated in PCs (L7Cre;Nf2$^{fl/fl}$), we found enlarged vGluT2-positive clusters in their presynaptic buttons together with increased amplitudes of miniature postsynaptic currents. The presynaptic terminals of these PCs innervating neurons of the deep cerebellar nuclei were also enlarged. When exploring mice with Merlin-deficient granule cells (GCs) (Math1Cre;Nf2$^{fl/fl}$), we found cerebellar extracts to contain higher amounts of vGluT1 present in parallel fiber terminals. In parallel, mEPSC frequency was increased in Math1Cre;Nf2$^{fl/fl}$ mice. On the contrary, VGluT2 clusters in cerebellar glomeruli composed of NF2-deficient presynaptic Mossy fiber terminals and NF2-deficient postsynaptic GC were reduced in size as shown for isoform-specific knockout mice. These changes in Math1Cre;Nf2$^{fl/fl}$-deficient mice were paralleled by an increased activation of Rac1–Cofilin signaling which is known to impact on cytoskeletal reorganization and synapse formation. Consistent with the observed synaptic alterations in these transgenic mice, we observed altered ultrasonic vocalization, which is known to rely on proper cerebellar function. No gross morphological changes or motor coordination deficits were observed in any of these transgenic mice. We therefore conclude that Merlin does not regulate overall cerebellar development, but impacts on pre- and post-synaptic terminal organization.

Keywords Cerebellum · Purkinje cell · Synaptogenesis · Neurofibromatosis type 2 · Ultrasonic vocalization

Introduction

Neuronal communication is critically dependent on synapses which translate electrical activity into chemical transmitter release. Understanding the molecular mechanisms underlying synapse formation and function is therefore a key aspect of neuronal development. The cerebellum is an excellent model for studying circuit connectivity because of its well-characterized and simple morphological architecture and its well-known synaptic network (Sassoe-Pognetto and Patrizi 2017; Ito 2002). Purkinje cells (PCs) are the central processing unit of the cerebellum which sums up all the inputs and transmits them to the deep cerebellar nuclei. Inputs are mainly provided by glutamatergic precerebellar climbing fibers and parallel fibers originating from granule cells (GCs) (Voogd and Glickstein 1998). PCs contain up to 200,000 synapses per cell which are innervated by different inputs and each synapse can act as an independent entity (Muller and Connor 1991). While climbing fibers form synapses at the thick, proximal PC dendrites, parallel fibers do so in the terminal PC branchlets (Palay and Chan-Palay 1974; Ichikawa et al. 2016). GCs are the most numerous cell type in the cerebellum and receive signals from Mossy fibers, Golgi cells and other neurons in multi-synaptic entities called glomeruli or rosettes, localized within the granular

✉ S. L. Baader
sbaader@uni-bonn.de

[1] Institute of Anatomy, Anatomy and Cell Biology, Bonn University, 53115 Bonn, Germany

[2] Institute of Physiology II, Bonn University, 53115 Bonn, Germany

[3] Leibniz Institute for Age Research, Fritz Lipmann Institute, 07745 Jena, Germany

cell layer just beneath the PC layer (Bahjaoui-Bouhaddi et al. 1997).

In a previous study, we showed that Merlin (the neurofibromatosis type 2 gene product) was expressed in cerebellar neurons during dendritogenesis and synaptogenesis (Schulz et al. 2010). We also demonstrated that Merlin affects process outgrowth in cultured neurons (Schulz et al. 2010). In addition, Merlin was upregulated in transgenic L7En-2 mice which showed delayed PC dendritogenesis (Holst et al. 2008; Jankowski et al. 2004). This raised the question whether Merlin might play a role during cerebellar development. In humans, complete loss of Merlin causes Neurofibromatosis type 2 which is typically characterized by tumor formation such as schwannomas, meningiomas, but is also associated with peripheral neuropathy (Ferner 2007). Although the role of Merlin in glial cells, particularly in Schwann cells, has extensively been characterized, Merlin's role in neuron development has not been explored in detail.

Expression of Merlin was initially shown in motoneurons of the spinal cord and cortical neurons (den Bakker et al. 1999; Huynh et al. 1996; Schulz et al. 2013a). Some of its known molecular properties support a function of Merlin in neuronal morphogenesis. It belongs to the Ezrin–Radixin–Moesin family of proteins that links cortical actin cytoskeleton to the plasma membrane (Li et al. 2012; McClatchey and Fehon 2009). Merlin regulation of actin cytoskeleton can take place by direct or indirect interaction with actin filaments, but mainly through its participation in signaling pathways mediated by the small GTPases Rac1 and RhoA (Morrison et al. 2007; Ramesh 2004; Shaw et al. 2001).

Merlin's activity can be regulated in multiple ways. First, two main isoforms of Merlin exist in mammals, which are distinguished by alternative C termini. NF2 isoform 1 is composed of 595 amino acids encoded by exons 1–15 and 17. NF2 isoform 2 instead contains exon 16 which bears a stop codon resulting in a slightly shorter protein (590 amino acids). Second, Merlin can be phosphorylated at multiple sites leading to changes in its folding state, binding partners and localization (Shaw et al. 2001; Kissil et al. 2002; Surace et al. 2004). The shortened protein NF2 isoform 2 lacks an important phosphorylation site considered to regulate Merlin activity (Gutmann et al. 1995).

Constitutive knockout of Merlin in mice was shown to be lethal at early embryonic stages (McClatchey et al. 1997). In order to study the relevance of Merlin function during cerebellar development, we used two mouse models in which either *isoform 1* or *2* has been deleted in all cells. In addition, we used conditional knockout mice, in which both Merlin variants were knocked out in either PCs using L7 promoter-driven Cre expression, or in GCs and Mossy fibers of the cerebellum by Math1 enhancer-driven Cre expression. By this conditional ablation of gene expression, we aimed to distinguish between cell-autonomous and non-cell-autonomous effects of Merlin. We report here a role of Merlin in fine-tuning synaptic connectivity and function.

Materials and methods

Animals

Mice of either sex used in this work were handled in strict adherence to local governmental and institutional animal care regulations (84-02.04.2016.A359, 84-02.04.2017.A120). Animals were housed under constant temperature and humidity conditions on a 12 h light/dark cycle, with access to food and water ad libitum. Animals older than 6 weeks were classified as adults. *Nf2* floxed animals (RIKEN BioResource Centre) were crossed with L7Cre-recombinase transgenic mice (JAX 004146, Barski et al. 2000) and Math-1Cre mice (Matei et al. 2005). NF2 iso1 (RBRC01870) and NF2 iso2 (RBRC01871) knockout animals generated by Dr. Michiko Niwakawakita and Dr. Marco Giovannini were purchased from RIKEN BioResource Centre (permission was given to H.M.). All animals were backcrossed at least ten times to a C57BL/6 background (Janvier-Labs, Paris, France).

Immunohistochemistry

Mice were deeply anesthetized with a mixture of Rompun (Bayer Vital GmbH, Leverkusen, Germany) and ketamine (WDT, Garbsen, Germany), and transcardially perfused using Ringer's solution, followed by 4% paraformaldehyde in phosphate buffered saline (PBS). Cerebella were dissected and immersion fixed overnight at 4 °C. After PBS washing, the samples were embedded in 2% agarose and 50-µm-thick sections were cut using a Leica vibratome (Microtome VT1000s, Leica, Wetzlar, Germany). For immunodetection, sections were washed in PBS, incubated in 10 mM sodium citrate solution, pH 6, at 80 °C for 30 min and then permeabilized with 0.5% TX-100 for 30 min. Blocking of unspecific sites was done by incubation in 0.2% gelatin and 1% goat serum in PBS at room temperature for 2 h. Primary antibodies dissolved in blocking solution were incubated at 4 °C overnight. The following antibodies were used: anti-Calbindin (mouse monoclonal antibody, 1:1000; Sigma-Aldrich, Germany, cat#C9848) anti-Calbindin (rabbit polyclonal antibody, 1:2000, Swant, Hamburg, Switzerland, cat#CB38), anti-Synaptobrevin (rabbit polyclonal antibody, 1:500, Synaptic Systems, cat#104202), anti-vGluT1 (mouse monoclonal antibodies, 1:500, Synaptic Systems, cat#135311), anti-vGluT2 (rabbit polyclonal antibody, 1:500, Synaptic Systems, cat#135402), anti-phospho-Histone H3 (Merck Millipore, Darmstadt, Germany,

cat#07-690), anti-NeuN (Merck Millipore, cat#MAB377), anti-activated caspase 3 (rabbit polyclonal antibody, 1:300; Cell Signaling, cat#9661). After three PBS washes, sections were incubated in the secondary antibody solution (Alexa Fluor 488 and 546 conjugated goat anti-mouse and anti-rabbit antibodies, 1:500 in blocking solution; Invitrogen, Darmstadt, Germany) at room temperature for 2 h. After PBS washing, sections were embedded in Slowfade gold mounting media (Thermo Scientific, Darmstadt, Germany).

Image acquisition and morphometry

Confocal images were acquired with a Leica TCS SP2 laser scanning microscope using 40 × 1.25NA and 63 × 1.4NA lenses. To avoid crosstalk between fluorophores, images were acquired sequentially using the 488- and 546-nm laser lines. Adobe Photoshop Elements 6.0 and 15.0 (Adobe Systems) and Fiji (Schindelin et al. 2012) were used for digital processing of images (brightness and contrast linear adjustments).

Measurement of dendritic spine density and length For dendritic spine density measurement, dendritic segments of at least the third order were chosen. In addition, we only chose regions in which single dendritic spines could be observed over a stretch of at least 50 µm. Since we only intended to compare wild-type and transgenic mice, we did not correct counts for potential oversampling (overlap of stacks in the *z* plane) or under sampling (spines elongated in the *z* plane could not be observed). Spine length was measured using the line drawing tool in ImageJ.

Measurement of vGluT puncta Size and quantity of vGluT2-positive puncta in the molecular (Figs. 2c, d, 6e) and internal granule cells layer (Fig. 9c) were measured by creating maximum intensity projections of 10 confocal sections (voxel size 0.37 × 0.37 × 0.16 µm). It should be noted that the numbers given are only meant to compare sizes and numbers between mouse genotypes, but not to provide absolute measures which is beyond the scope of fluorescent microscopy. A minimum fluorescence threshold was applied to the projections and the image was then transformed into a binary format using plugins of Fiji. Size and density of the puncta were measured with the Analyze Particle algorithm. For vGluT2 measurements within the IGL, only clusters in between 5 and 25 µm^2 were included, since imaging did not allow to clearly separate all clusters, and in order to avoid background counting.

VGluT distribution pattern For measuring the distribution of vGluT2 puncta within the molecular layer (Fig. 9e), confocal images were acquired using a 40× oil immersion objective and a pinhole of 0.5 airy units (voxel size 0.092 × 0.092 × 0.5 µm). Images were taken every 0.5 µm along a 5-µm-thick optical *z* axis. Maximum projections were then generated, and the vGluT2 channel was selected for plot profiling. VGluT2 density profiling within the molecular layer was done by marking a rectangular region of interest (ROI) spanning the whole dendritic tree from the PC layer to the pia. Then, an intensity profile along the PC layer–pia axis was created using the plot profile function of Fiji-ImageJ (v. 1.52i). Using R statistic software, intensity profiles were normalized to account for variable molecular layer thicknesses by adapting intensity profiles to the maximum PC layer–pia distance obtained. Five ROIs from the anterior lobe were analyzed per mouse, three mice were used per genotype. Cumulative sums were calculated from the mean intensities derived from each animal and sums were normalized for maximum intensities to account for staining variability's. A summarized *t* test was done using the tsum.test statistics provided by the PASWR2 package of R. The distribution of vGluT1 puncta within the molecular layer was analyzed accordingly using a single *z* plane of 0.5 µm in thickness. It should be noted that this procedure only addresses the distribution of vGluT1 and vGluT2 along the PC layer to pia axis, but does not allow for judging expression levels.

Measurement of axonal terminals PC axon terminals were encircled manually and the area measured using Fiji tools. To ensure unprejudiced measurements samples have been evaluated by two different experimentators not knowing the genotype of the originating mice.

Infraganglionic axonal complexity was evaluated by measuring all pixels within a 20-µm-thick area beneath the PC layer in images taken from Calbindin-stained vibratome sections. Values are given as stained areas per 100 µm^2.

Western blot

Tissue samples were lysed in RIPA buffer (20 mM Tris–HCl pH 7.5, 150 mM NaCl, 1 mM EDTA, 1 mM EGTA, 1% NP-40, 1% sodium deoxycholate) supplemented with protease inhibitors (Pefabloc, Sigma-Aldrich). Protein concentrations were determined with BCA™ kit (Thermo Scientific). Equal amounts of protein were loaded and separated by SDS-PAGE in a 12% polyacrylamide gel. Proteins were then transferred to a polyvinylidene fluoride membrane (Millipore, Darmstadt, Germany) using a semidry transfer system (Nova Blot, GE Healthcare, Munich, Germany). Unspecific binding sites on the membrane were blocked with 5% milk resuspended in 0.1% Tween-20 in PBS for 2 h. Primary antibodies were diluted in blocking solution and incubated overnight at 4 °C (anti-NF2 clone A19, rabbit polyclonal antibody, 1:500, Santa Cruz Biotechnology Inc., Heidelberg, Germany; anti-β-actin-HRP antibody, 1:4000, Santa Cruz Biotechnology; anti-PSD-95, mouse monoclonal antibody 1:2000, Thermo Scientific, cat#MA1-046; anti-Homer1, rabbit polyclonal antibody, 1:5000, Synaptic Systems, cat#1160002; anti-Synaptophysin, rabbit polyclonal antibody, 1:2000; Abcam, cat#ab32594; anti-vGluT1 and

anti-vGluT2, rabbit polyclonal antibodies, 1:1000, Synaptic Systems, cat#135302, 135402; anti-Cofilin, mouse monoclonal antibody, 1:5000, BD Transduction Laboratories, cat#612144; anti-phospho-Cofilin, rabbit polyclonal antibody, 1:2000, Cell Signaling, cat#3311; anti-Cyclophilin B, rabbit polyclonal antibody, 1:8000, Abcam, cat#ab16045). After three washes in 0.1% Tween-20 in PBS for 15 min, membranes were incubated with the secondary antibody diluted in blocking solution for 2 h at room temperature (goat anti-mouse or anti-rabbit HRP, 1:8000, Dako, Hamburg, Germany). Immunoreactive bands were visualized using SuperSignal® West Pico or FemtoChemoluminescent Substrate (Thermo Scientific). Each experiment was repeated at least three times. Optical density measurements of whole bands were performed using the Image J (NIH) Gel analysis plugin. Results were normalized using β-actin or cyclophilin B (as indicated in each figure).

Primary cell cultures

GCs were obtained from 8-day-old pups and prepared as previously described (Baader and Schilling 1996). Briefly, GCs were dissociated using 10 mg/ml trypsin and triturated to remove cellular aggregates. Cells were then plated at a density of 40,000 cells/cm^2 on poly-L-lysine coated slides (20 µg/ml) in Neurobasal culture medium supplemented with B27 (Invitrogen) and 2 mM glutamine (Invitrogen). Cultures were fixed after 8, 12, and 24 h in 4% paraformaldehyde (PFA).

PC cultures were prepared from mouse embryos at embryonic day 17.5. Briefly, embryos were removed by cesarean-section from pregnant mice and killed by decapitation. The cerebella were dissected and kept in Hank's balanced salt solution. After meninges removal, cerebella were chopped and incubated in trypsin 10 mg/ml for 15 min and dissociated with gentle pipetting. Cell suspension was then centrifuged at 1300 rpm, for 5 min. After careful removal of the supernatant, cells were resuspended in Neurobasal culture medium supplemented with B27 (Invitrogen) and 2 mM glutamine (Invitrogen). Cells were counted and seeded on (20 µg/ml) poly-L-lysine and laminin-coated slides.

Immunocytochemistry

After fixation, cells were permeabilized with 0.1% Triton X-100 for 3 min. Non-specific antibody binding sites were blocked using 1% bovine serum albumin and 10% goat serum for 30 min. Incubation with the primary antibodies in blocking solution at 4 °C was carried out overnight. The following primary antibodies were used: anti-βIII Tubulin (rabbit polyclonal antibody, 1:500, Sigma-Aldrich, cat#T2200), anti-acetylated Tubulin antibody (mouse monoclonal antibody 1:250, Sigma-Aldrich, cat#T5192) and anti-Calbindin antibody (rabbit polyclonal antibody, 1:2000; Swant, cat#CB38). After extensive rinsing in PBS, cells were incubated with goat anti-mouse or anti-rabbit secondary antibodies linked to Alexa Fluor-488 and 546 (1:500; Invitrogen) for 1 h. Afterwards, cells were counterstained with Hoechst 34580 (1 µg/ml in PBS, Invitrogen) for 20 min. Slides were mounted in Slowfade gold (Invitrogen).

Quantitative PCR (qPCR)

Total RNA was isolated from cerebella of P8, and adult NF2 iso1 and iso2 knockout, heterozygote and wild-type mice using Trizol reagent following the manufacturer's instructions (Life Technologies, Ober-Olm, Germany). 50 ng of diluted RNA was reverse-transcribed using the iScript cDNA Synthesis Kit (BioRad, Munich, Germany). The cDNA was diluted to 2.5 ng/µl and assayed in 10-µl PCR reactions. The sequence-specific Taqman primers for *Nf2 iso1* (Assay ID: Mm0187735_m1) and *Nf2 iso2* (Mm0187750_m1) were purchased from Life Technologies. *Gapdh* (Mm99999915_g1) and *Atp5b* (Mm01160389_g1) were used as reference genes. A no-template control (NTC) of water was assayed along with cDNA samples. Each gene was assayed on Bio-Rad Hard-Shell Plates (BioRad) containing triplicate wells of cDNA from all samples. Each qPCR reaction contained the following: 5 µl PCR master mix (TaqMan Gene Expression Master Mix, Life Technologies), 0.5 µl of each primer set, and 3 µl of cDNA. All qPCR reactions were carried out on CFX96 Touch Real-Time PCR Detection System (Bio-Rad). The thermal cycling parameters used were as follows: 2 min incubation at 50 °C, 10 min initial denaturation at 95 °C, followed by 40 cycles of two-step amplification at 95 °C for 15 s and 60 °C for 60 s, and a final incubation for 30 s at 65 °C. Technical replicates (triplicates) of *C*q values for each sample were combined in a single mean value and then further analyzed by the method of Pfaffl (2001). Expression levels are given as relative amounts to those of *Gapdh* and *Atp5b*.

Golgi staining

Golgi staining was performed on P9 and adult cerebellum using the FD Rapid GolgiStain kit (FD Neurotechnologies, Ellicott City, MD, USA) according the manufacturer's instructions. Two to three cerebella from each genotype and age were processed. Stained cerebella were embedded in Tissue-Tek O.C.T (Sakura Sinetek, Leiden, Netherlands) and sectioned at 140 µm. After staining and mounting, images were acquired using an Axioskop 2 microscope equipped with a Cool Snap EZ digital camera (Visitron Systems, Puchheim, Germany) and Axio Vision 4.8.2.0 software (Carl Zeiss MicroImaging GmbH, Jena, Germany). *Z* stacks at 1 µm interval were taken from PCs aligning the fissure

between lobule 3 and 4. Sholl analysis was done using Fiji software (Schindelin et al. 2012; Ferreira et al. 2014).

Cresyl violet staining

Sections were colored in a solution containing 1% cresyl violet and 1% thionine for 3 min and then differentiated on 80% ethanol and acetic acid. After washing in tap water, sections were dehydrated and mounted in Depex.

Electrophysiology

Mice at the age of 4–6 weeks were used for measuring miniature excitatory postsynaptic currents (mEPSCs). Mice were deeply anesthetized with isoflurane, decapitated, and the cerebellum was chilled for 1 min in an ice-cold solution containing 234 mM sucrose, 2.5 mM KCl, 1.25 mM NaH_2PO_4, 26 mM $NaHCO_3$, 0.5 mM $CaCl_2$, 10 mM $MgSO_4$, and 11 mM D-glucose (pH 7.4). The solution was saturated with carbogen (95% O_2 and 5% CO_2). Sagittal cerebellar slices of the vermis of 200 µm thickness were prepared in this solution using a Leica vibratome (VT 1200S). Sections were subsequently equilibrated in a custom-made chamber submerged in artificial cerebrospinal fluid (ACSF; 120 mM NaCl, 2.5 mM KCl, 1.25 mM NaH_2PO_4, 26 mM $NaHCO_3$, 2 mM $CaCl_2$, 1 mM $MgCl_2$, 17 mM D-glucose; pH 7.4) continuously gassed with carbogen for 30 min at 35 °C. Then, slices were kept at RT.

Slices were constantly superfused with gassed ACSF. PCs located along the primary fissure in between lobules V and VI were visualized by differential infrared video microscopy (BX51, Olympus, Tokyo, Japan). Recording electrodes had a resistance of 2.5–3.5 MΩ pulled from borosilicate glass (Science Products, Hofheim, Germany). The internal solution contained (in mM): 150 Cs-gluconate, 8 NaCl, 2 MgATP, 10 HEPES and 0.2 EGTA, pH 7.2, 290 mOsm/kg. MEPSCs were recorded in voltage clamp at − 70 mV in ACSF supplemented with tetrodotoxin (TTX, 0.5 µM, Tocris Bioscience, Bristol, UK) and picrotoxin (PTX, 100 µM, Sigma-Aldrich, Taufkirchen, Germany). Data were acquired using a Multiclamp 700B amplifier (Axon Instruments, Sunnyvale, CA), digitized with a Digidata 1322A (Axon Instruments, Union City, CA), and stored on a PC. mEPSCs were detected offline and statistically analyzed with a custom-written Matlab routine (MathWorks, Aachen, Germany). Statistical analyses of cumulative distributions were performed applying the Kolmogorov–Smirnov test. Recordings and analyses were performed by an investigator blinded to the genotype.

Behavioral tests

Motor coordination was assessed in 2-month-old male using Rotarod (Ugo Basile, Genomio, Italy) for 5 consecutive days giving the mice four trials each day with intervals of 30 min. Mice were placed on an accelerating rod which initially rotated at 4 rpm and accelerated to 40 rpm within 300 s. The time being on the rod was measured (latency to fall). Mice that did not move but rotated along with the rod were excluded from the ongoing analysis. Differences in times to fall were statistically evaluated by Shapiro–Wilk test followed by a Student's *t* test for each day and by two-way ANOVA summarizing data for all days.

Ultrasonic sounds of 6-day-old pups were recorded using Avisoft-UltraSoundGate 116Hb and a condenser microphone (sensitive to frequencies between 10 and 180 kHz) and evaluated by the Avisoft-SASLab Pro software (Avisoft Bioacoustics, Berlin, Germany). For recording, each pup was placed into a plastic container located in a sound-attenuating Styrofoam box which was covered by a lid containing the Microphone. Recordings were made using Avisoft Recorder Software (Version 3.2) at a sampling rate of 250 kHz. For analysis recordings, data were transferred to the Avisoft-SASLab Pro (Version 4.40) and a Fast Fourier Transformation was conducted. Spectrograms were produced at a frequency resolution of 488 Hz and a time resolution of 1 ms. A lower cut-off frequency of 40 kHz was used to reduce background, call detection parameters used were as follows: minimum duration 3 ms, hold time 20 ms, element postfilter: minimum duration 2 ms and maximum entropy 0.9. Peaks were rejected if the amplitude was lower than − 50 dB. Waveform patterns were classified in nine categories based on internal pitch changes, lengths and shapes according as published previously (Scattoni et al. 2008).

Experimental design and statistical analysis

For immunohistochemical analysis, at least three mice per genotype were analyzed. For each mouse, at least two slices and at least three regions of interest per slice located in lobule IV were evaluated. Measurements of molecular layer thickness or synaptic dot sizes were based on these regions of interest. PC diameters were measured on at least 10 PCs per section in the medial region of lobule IV (2 ROIs with an area of 375×375 µm^2). Differences in the complexity of the infraganglionic plexus were evaluated on at least five regions of interest derived from five sections and three mice. For Golgi staining analysis, three brains from mice of each genotype and age derived from different litters were stained and at least five PCs were selected from each mouse brain to perform Sholl analysis. Cumulative crossings were calculated and fitted to a sigmoid curve (using the self-starting nonlinear-least squares logistic model provided in the SSlogic function of R statistics). Data for genotypes have been compared by the Kolmogorov–Smirnov test. Electrophysiological measurements were done on at least three mice measuring at least 5 PCs per mouse. Cumulative probabilities

of mEPSCs were compared by Kolmogorov–Smirnov testing. For morphological analysis of cultured neurons, three preparations of a mixture of at least three mice for each genotype were used. Behavioral studies were done with at least 13 mice. Performance of mice on Rotarod experiments were compared by linear regression analysis while single time points were compared by Student's *t* test. Calls/min, interval durations and durations of calls were compared by Wilcoxon's ranking test. Numbers of classified calls were compared by linear regression while the duration of these calls was statistically evaluated by paired Student's *t* test. All statistics were done using either GraphPad Prism version 6 (GraphPad Software, LaJolla, USA) or R (R Development Core Team 2008). Equality of variances were checked by Levene's test statistic, and test for normality distributions was done by Shapiro–Wilk test. If homogeneity of group variances and normality distribution was shown, inter-group comparisons were done by Student's *t* test. For multiple comparisons, data were analyzed by two-way ANOVA with Bonferroni's post-test. Non-parametrically distributed data were compared by Wilcoxon rank test or by linear regression modeling. Details for each test are given in the legends. Data are presented as mean ± SEM. Significances were set as $*p<0.05$; $**p<0.01$; $***p<0.001$. Exact values are given in figure legends.

Results

Morphological consequences of Merlin deficiency in isoform-specific knockout mice

Given the spatiotemporal expression patterns of NF2 isoforms 1 and 2 and a function of NF2 isoform 1 in process outgrowth in vitro, we hypothesized that Merlin is important for the transition from immature to mature neurons in the central nervous system (CNS). In order to experimentally address this issue, we first used isoform-specific knockout mice which had turned out to be a valuable tool to investigate Merlin's function in vivo (Schulz et al. 2013a).

Both isoform-specific knockout mice were viable and fertile, and did not show gross abnormalities in cerebellar morphology. Sholl analysis of Golgi-impregnated adult cerebellar sections demonstrated that PCs of NF2 isoform 1 and isoform 2 mutants displayed less dendritic branches starting at about 80 µm from the soma as compared to wild-type PCs (Fig. 1a, b). These differences in the branching pattern are statistically significant accounting for a 17% reduction in NF2 isoform 1-deficient mice and for 9% in NF2 isoform 2-deficient mice. In order to avoid analyzing alterations in branching caused by differences in the mouse background strain, we always used litter mates for our analysis. Having seen alterations in dendritic branching, we analyzed

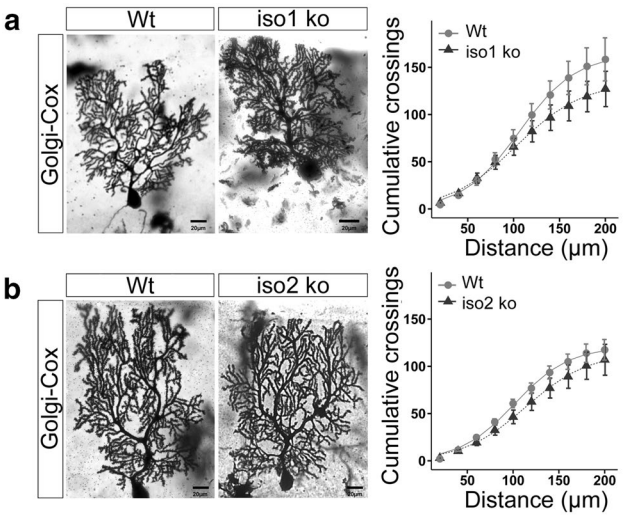

Fig. 1 Isoform-specific NF2 knockout mice show reduced PC complexity. **a**, **b** Images represent typical Golgi-stained adult PCs from lobule IV in NF2 iso1 (**a**) and NF2 iso2 (**b**) mice. Line plots show the results of Sholl analyses presented as mean cumulative crossings of PC dendrites with circles at regular distances around the soma. Error bars mark standard errors (**a** $n_{PC,\ Wt}=10$, $n_{PC,\ NF2\ iso1}=10$, $p=0.0061$; **b** $n_{PC,\ Wt}=24$, $n_{PC,\ NF2\ iso2}=16$, $p=0.0179$; Kolmogorov–Smirnov)

morphological parameters of dendritic spines. No differences in dendritic spine densities could be observed between PCs of *Nf2 Isoform1* and *Isoform 2* knockout as compared to corresponding control mice (Fig. 2a, b). Identifiable spines of NF2 iso1 and iso2 knockout and corresponding wild-type PCs were both in the range of 900 nm in length (Fig. 2a, b). In both transgenic mice, we could demonstrate a difference in spine length between wild-type and transgenic PCs in the range of 5–10%. Interestingly, however, NF2 isoform 1 mutants revealed a decrease in spine length, while NF2 isoform 2 mutants displayed an increase. This difference in spine length after isoform 1 or 2 deficiency is in line with the notion that isoforms 1 and 2 differ in protein conformation and in functional properties (Sher et al. 2012; Xing et al. 2017). Again, we noted a difference in spine length of PCs between Nf2 isoform 1 and isoform 2 wild-type mice quoting for strain differences. Therefore, we only compared litter mates and PCs of corresponding locations along the rostrocaudal axis of corresponding wild-type and Merlin knockout cerebella. To assess a possible effect of Merlin in synapse morphology in more detail, we immunohistochemically stained cerebellar sections with vGluT2 or vGluT1 antibodies which specifically label presynaptic terminals of climbing and parallel fibers present on PCs, respectively. We found that, although the number of vGluT2 puncta was unchanged, the cerebellar tissue of Nf2 iso1 and iso2 knockout mice showed smaller vGluT2 puncta than wild-type mice (Fig. 2c, d). This correlates with a decrease in the amplitude of miniature excitatory postsynaptic currents (mEPSCs)

measured at PCs of Merlin knockout mice by patch clamp (NF2 iso1: 13.28 ± 0.23 pA, $n = 15$ vs. Wt: 14.56 ± 0.42 pA, $n = 16$, KS test $p < 0.001$; NF2 iso2: 12.58 ± 0.15 pA, $n = 18$ vs. Wt: 13.61 ± 0.19 pA, $n = 29$, KS test $p < 0.001$; Fig. 2e, f). The mEPSCs frequency was significantly decreased in Merlin knockout mice as compared to wild-type littermates (NF2 iso1: 0.96 ± 0.11 Hz, $n = 15$ vs. Wt: 1.23 ± 0.14 Hz, $n = 16$, KS test $p < 0.001$; NF2 iso2: 0.72 ± 0.09 Hz, $n = 18$ vs. Wt: 1.12 ± 0.16 Hz, $n = 29$, KS test $p < 0.001$). Since the amplitude was decreased, we cannot rule out that the decrease in mEPSC frequency might be due to an increased number of subthreshold mEPSCs. However, we can show that alterations in vGluT2-stained terminals were paralleled by changes in electrophysiological properties in cerebellar PCs. We thus conclude that manipulating NF2 expression affects climbing fiber to PC connectivity.

Previously, it has been shown, that NF2 isoform-specific knockout mice showed compensatory overexpression of the remaining isoform in the male reproductive system (Zoch et al. 2015). We therefore measured *Nf2 isoform 1* and *isoform 2* expression in cerebellar extracts of mice at postnatal day 8 and of adult mice by quantitative PCR, and found a complete absence of the genetically ablated *isoform* (Fig. 2g, h). However, there was a clear upregulation of the corresponding alternative *isoform* at postnatal day 8, i.e., the deletion of *Nf2 isoform 1* caused a complete elimination of *isoform 1* expression, as expected, but a temporal overexpression of *Nf2 isoform 2*. Vice versa, we observed a temporally restricted overexpression of *isoform 1* in Nf2 isoform 2 knockout mice (Fig. 2g, h). It is thus not clear whether the observed morphological and physiological alterations were due to depletion of an *NF2 isoform* or to a developmental early overexpression of the remaining isoform.

In order to assess this question and to clarify whether the effects observed in Merlin isoform-specific knockout mice were cell-autonomous, we used conditional knockout mice in which *Nf2* was specifically deleted in granule cells or Purkinje neurons.

Merlin deficiency in granule cells enhances neurite growth in vitro

Conditional knockout mice for GCs were generated by crossing $Nf2^{fl/fl}$ mice to Math1-Cre mice. These mice express Cre recombinase in GCs within the cerebellar cortex and in pontine neurons which project to the cerebellar cortex as Mossy fibers. Its expression starts at a time when GCs begin to proliferate (Gliem et al. 2006). Dissociated GC cultures derived from 8-day-old Math1Cre;$Nf2^{fl/fl}$ mouse pups showed reduced Merlin expression by more than 90% ($p = 0.047$; Fig. 3c). Math1-driven gene expression starts at embryonic stages and extends from the anterior lobe to the posterior lobule IX until P8, thus covering most of the cerebellar granule cells (Pan et al. 2009). Since it has been shown that Merlin deficiency enhances process outgrowth in cell lines (Schulz et al. 2010), we tested process formation and growth in primary cultures of GC derived from conditional knockout mice. Cultured GCs were stained for acetylated tubulin after 8 and 12 h in culture to ensure identification of single processes (Fig. 3a). Most of the long visible neurites were considered to correspond to axons, because dendrites take about 5–6 days to grow in vitro (Powell et al. 1997). 80% of the cells had no processes at 8 h in vitro, both in wild-type and Math1Cre;$Nf2^{fl/fl}$ mice. However, at this early stage process forming neurons in cultures derived from Math1Cre;$Nf2^{fl/fl}$ consistently showed ~ 27% longer neurites (34.8 ± 2.5 µm) than those from wild-type mice (27.3 ± 1.6 µm, $p = 0.02$, mean ± SEM). After 12 h in culture, ~ 80% of the cells showed 1 or 2 processes independent of the genotype. Again, neurites were ~ 18% longer on average in the NF2-deficient than wild-type neurons (Wt;$Nf2^{fl/fl}$:34.7 ± 1.7 µm, Math1Cre;$Nf2^{fl/fl}$: 40.9 ± 2.2 µm; $p = 0.03$, mean ± SEM; Fig. 3b).

Rho GTPases are known regulators of neurite growth. Particularly, Rac1 activation leads to p21-activated kinase-mediated phosphorylation of Cofilin and thus F-actin stabilization (Kuhn et al. 2000; Ng and Luo 2004). Since Merlin inactivates Rac1, it reduces actin stabilization mediated by Rac1 (Morrison et al. 2007). Merlin deficiency might therefore result in a Cofilin-dependent stabilization of actin cytoskeleton and thus stabilization of processes (Avery et al. 2017; Borovac et al. 2018). To test this hypothesis, we analyzed Cofilin phosphorylation in Math1Cre;$Nf2^{fl/fl}$ mice and found a significant increase in Cofilin phosphorylation at Ser3 (Fig. 3c). P-Cofilin was localized to cell bodies and axons from GCs, including growth cones (Fig. 3d). It is therefore plausible, that Merlin suppresses process outgrowth in cultured GCs by a Cofilin-dependent mechanism.

Merlin deficiency in cultured Purkinje cells promotes dendritic growth

Since Merlin was shown to be expressed in cerebellar PCs in a temporal pattern resembling neuronal differentiation (Schulz et al. 2010), we next analyzed PC morphology in culture to evidence changes in axonal and dendritic morphology. To this end, we used transgenic mice in which part of the *Nf2* gene was excised specifically in cerebellar PCs using the L7/pcp-2 promoter (Barski et al. 2000). Cultures were prepared from cerebella of 17.5-day-old embryos and incubated for 8 days in vitro (*div*) before analysis. In such cultures established at this age, L7/Pcp-2 promoter activity was shown before (Schilling et al. 1991). Consistently, using RT-PCR, we found a clear signal at the band size expected for Cre in cerebella of mice from which the cultures were established (Fig. 4e).

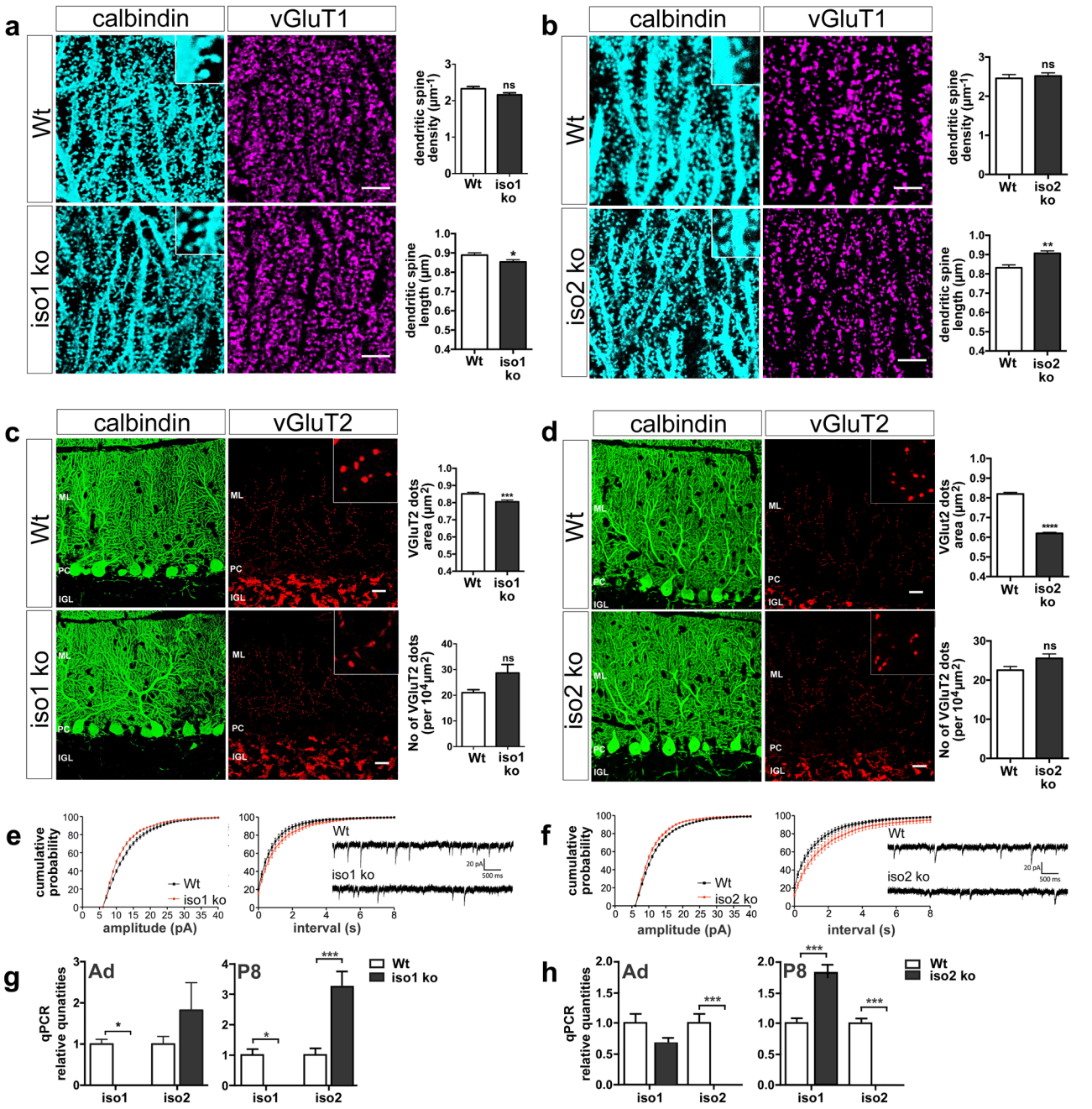

Cultured PCs were identified by Calbindin 1 immunocytochemistry, and comparable numbers of Calbindin-positive cells were found in cultures obtained from wild-type and L7Cre;Nf2$^{fl/fl}$ mice. Imaging and reconstruction of the cell processes revealed that PCs of Merlin-deficient mice had dendrites ~ 15% longer than those of wild-type mice (Wt;Nf2$^{fl/fl}$ 3.61 ± 0.1 µm, L7Cre;Nf2$^{fl/fl}$ 4.70 ± 0.11 µm, $p = 0.003$; Fig. 4a, b). Axons, which can be readily discerned as processes that are extremely long, thin and of uniform thickness (Baptista et al. 1994) were excluded from measurements. The number of dendritic branching points found per PC and the number of processes derived from a soma were unchanged in L7Cre;Nf2$^{fl/fl}$ PCs compared to wild-type cells (Fig. 4c, d). As for cultured GCs, we can conclude that Merlin is a negative regulator of process outgrowth in cultured PCs.

Merlin deficiency reduces dendritic branching in cerebellar Purkinje cells in vivo

Since process formation of PCs was affected in vitro by Merlin deficiency, we next investigated dendrite formation

◂**Fig. 2** NF2 isoform 1 and 2-specific knockout affect synaptic size and activity. **a** Confocal images of PC dendrites located in lobule IV derived from adult NF2 iso1$^{+/+}$ (Wt) and NF2 iso1$^{-/-}$ (iso1 ko) mice, double stained for Calbindin (cyan) and vGluT1 (magenta). Scale bar: 5 µm. Insets represent enlargements of Calbindin stainings to demonstrate details of dendritic spines. Bar plots represent spine densities and lengths. Bars depict mean ± SEM from three animals per genotype (spine density: $p_{\text{density}} = 0.057$, $n_{\text{density, Wt}} = 48$, $n_{\text{density, NF2 iso1}} = 40$; $^{*}p_{\text{spines}} = 0.047$, $n_{\text{spines, Wt}} = 200$, $n_{\text{spines, NF2 iso1}} = 220$, Mann–Whitney Wilcoxon test). **b** Stainings and evaluations of NF2 iso2 spines were done as described in **a**. While spine density was unchanged ($p_{\text{density}} = 0.87$, $n_{\text{density, Wt}} = 42$, $n_{\text{density, NF2 iso2}} = 43$, Mann–Whitney Wilcoxon test), spine length was significantly increased in iso2 ko mice ($^{**}p_{\text{spine length}} = 0.0014$, $n_{\text{Wt}} = 74$, $n_{\text{NF2 iso1}} = 49$, Mann–Whitney Wilcoxon test). **c** Confocal images of PCs derived from Wt and NF2 iso1 ko mice, double stained for Calbindin (green) and vGluT2 (red). *ML* molecular layer, *PC* Purkinje cell layer, *IGL* inner granule cell layer. Scale bar: 20 µm. Insets represent enlargements of vGluT2-stained dots. Bar plots represent sizes and densities of vGluT2-positive puncta in the molecular layer. Bars depict mean ± SEM from three animals per genotype ($^{***}p_{\text{area}} \leq 0.001$; $n_{\text{Wt}} > 6800$, $n_{\text{NF2 iso1}} > 8500$, Mann–Whitney Wilcoxon test). **d** Stainings and evaluations of NF2 iso2 spines were done as described in **c** ($^{***}p_{\text{area}} < 0.001$; $n_{\text{Wt}} > 7300$, $n_{\text{NF2 iso2}} > 96{,}000$, Mann–Whitney Wilcoxon test). **e** Cumulative distribution plots of mEPSC amplitudes (left) and mEPSC inter-event intervals (middle) from NF2 iso1 knockout mice (iso1 ko) and wild-type (Wt) littermates. Right: mEPSC sample traces. **f** Cumulative distribution plots of mEPSC amplitudes (left) and mEPSC inter-event intervals (middle) from NF2 iso2 knockout (iso2 ko) mice and wild-type (Wt) littermates. Right: mEPSC sample traces. The knockout of either NF2 isoform 1 or 2 results in a decrease of mEPSC amplitudes and frequencies compared to wild-type littermates. **g**, **h** Relative expression of NF2 isoform 1 and 2 in adult (Ad) and 8-day-old (P8) isoform-1 (**g**) and 2 (**h**) knockout mice as evaluated by qPCR. Expression levels were related to ATP5b and GAPDH expression (three independent samples per genotype)

and axonogenesis in vivo. Again L7Cre;Nf2$^{fl/fl}$ mice were used to reduce Merlin expression specifically in PCs. Cre expression driven by the L7/pcp-2 promoter was detected in L7Cre;Nf2$^{fl/fl}$ mice as early as postnatal day 0 (Fig. 5c) and was present up into adulthood (Fig. 5c, e), while it was absent in wild-type mice.

Looking at the size, lobulation and layering of the cerebellum, we did not detect any alterations in Merlin-deficient mice (Fig. 5a). We also did not observe a difference in PC density and monolayer formation between genotypes, suggesting that cell proliferation and/or survival were unchanged (Fig. 5a). We then measured the thickness of the molecular layer, which is a good indicator of developmental and disease-associated defects that disrupt PCs (Hansen et al. 2012; White et al. 2014). At early postnatal stages (P8) the molecular layer of L7Cre;Nf2$^{fl/fl}$ mice was significantly narrower (95.1 ± 2.1 µm, $n = 40$) than that of wild-type mice (114.5 ± 2.1 µm, $n = 40$; $p < 0.001$; Fig. 5b, c). This shortened molecular layer was persistently found into adulthood being 191.8 ± 2.2 µm in L7Cre;Nf2$^{fl/fl}$ and 209.1 ± 0.8 µm in control mice ($n = 40$ neurons, $p < 0.001$; Fig. 5d, e). The diameter of the PC somata was reduced in adult knockout mice by only 6% (17.3 ± 0.3 µm in L7Cre;Nf2$^{fl/fl}$ mice vs. 18.4 ± 0.3 µm in Wt;Nf2$^{fl/fl}$ mice, $n = 70$ neurons; $p < 0.047$; Fig. 5e).

This result was surprising given the in vitro observations in which Merlin deficiency promoted process outgrowth. We therefore tested whether dendrite branching patterns were affected by Merlin deficiency in vivo, assuming that reduced branching might affect dendritic tree size. Adult cerebellar sections of either genotype were stained with the Golgi technique, and the complexity of the dendritic tree was quantified by Sholl analysis (Sholl 1953). In P9 animals, we observed no difference in the branching pattern of PCs between L7Cre; Nf2$^{fl/fl}$ and Wt mice. In older PCs, a significant shift of the number of intersections towards smaller distances from the soma was observed. Dendrites branched closer to the soma (the inflection point of the sigmoid curve is shifted to the left in Fig. 5g), and the number of crossings in the distal part was reduced by about ~ 15% in L7Cre;Nf2$^{fl/fl}$ as compared to Wt;Nf2$^{fl/fl}$ PCs (Fig. 5g). We also measured the width of PCs in knockout and wild-type mice, but did not see a difference (155 ± 5 µm vs. 144 ± 9 µm in Wt and L7Cre;Nf2$^{fl/fl}$ mice; $n_{\text{Wt}} = 20$, $n_{\text{PC ko}} = 16$). Similarly, proximal segment lengths obtained from Golgi-impregnated PCs did not reveal changes in segment length (24 ± 2 µm vs. 26 ± 5 µm). This led us to conclude that Merlin deficiency caused a change in the branching pattern in cerebellar PCs in vivo, while it increased dendritic growth in cultured neurons.

Merlin deficiency in Purkinje cells affects morphological and electrophysiological features of synaptic terminals

Since L7 promoter-driven excision of the *Nf2* segment is restricted to PCs, we assumed that Merlin deficiency primarily affects the postsynaptic side. Using a panel of antibodies, we first studied the overall expression level of different synaptic markers in total cerebellar extracts of Wt;Nf2$^{fl/fl}$ and L7cre;Nf2$^{fl/fl}$ mice. Both postsynaptic (PSD-95 and Homer-1) and presynaptic proteins (synaptobrevin, synaptophysin, vGluT1, vGluT2) were expressed in comparable quantities in both genotypes (Fig. 6a). The only significant reduction measured applied to Merlin expression. It was reduced by ~ 53%, which is a reasonable percentage considering the conditional PC-specific knockout approach. In order to address a possible effect of Merlin in synapse formation, we immunostained cerebellar sections from littermate control and L7Cre;Nf2$^{fl/fl}$ animals using vGluT2 or vGluT1 antibodies (Fig. 6c, d). The average number of vGluT2-positive synaptic boutons per 10,000 µm^2 was comparable in both genotypes (Fig. 6c, e), the average size of vGluT2-positive boutons was, however, significantly increased in L7Cre;Nf2$^{fl/fl}$ vs. wild-type PCs (Wt: 0.84 ± 0.02 µm^2; PC

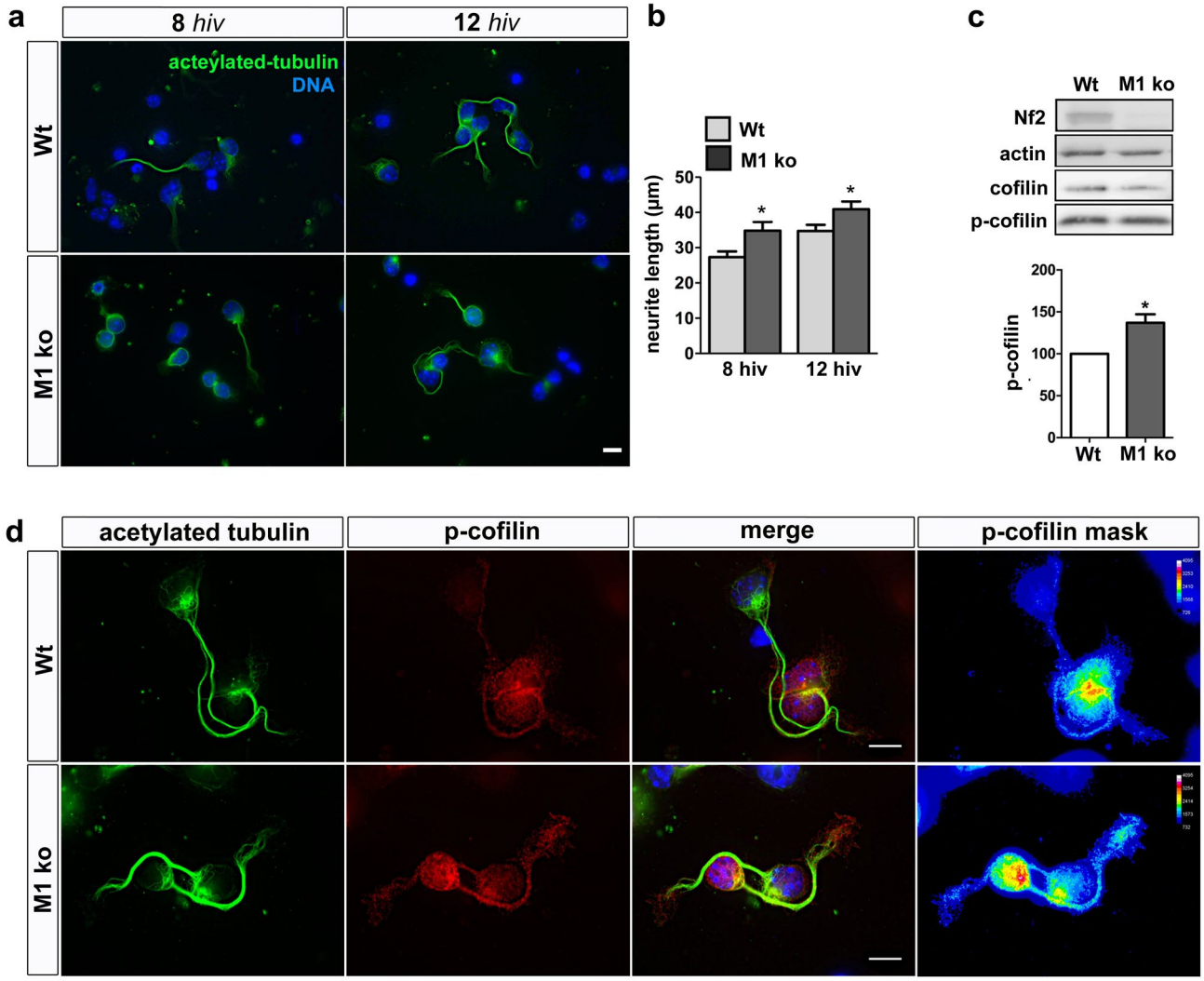

Fig. 3 Merlin knockout in granule cells increases axonal growth in culture. **a** Images of granule cell cultures prepared from cerebella of 8-day-old Wt;Nf2$^{fl/fl}$ (Wt) and Math1Cre;Nf2$^{fl/fl}$ (M1 ko) mice, maintained for 8 and 12 h in vitro (*hiv*) and immunostained with antibodies against acetylated tubulin. Scale bar: 10 µm. **b,** Neurite lengths were measured, and bars depict mean ± SEM from three independent experiments (*$p_{8\ hiv} \leq 0.02$, $n_{Wt} = 45$, $n_{PC\ ko} = 33$; $p_{12\ hiv} = 0.03$, $n_{Wt} = 67$, $n_{PC\ ko} = 68$; Mann–Whitney Wilcoxon test). **c** Western blot of extracts derived from granule cell cultures of Wt and M1 ko cerebella. Values for bar plots represent mean ± SEM (*$p = 0.047$, Student's *t* test, $n = 3$). **d** Phospho-Cofilin/acetylated Tubulin double staining of granule cells cultured for 24 h. Phospho-Cofilin intensity was color coded in the right image showing its localization along axons and in growth cones. Scale bar = 10 µm

ko: 0.90 ± 0.03 µm^2; $n > 6000$; $p < 0.001$). This indicates alterations in the climbing fiber terminals on PC dendrites at the presynaptic side. VGluT1-positive puncta were so numerous within the molecular layer that we could not reliably measure their size and number. Since almost all of the vGluT1-positive puncta are derived from granule cells innervating PC dendritic spines (Hioki et al. 2003), and since spine density was comparable between genotypes (Fig. 6f), it is fair to assume that numbers of vGluT1 puncta are comparable in both genotypes. VGluT2 data, however, suggest that postsynaptic Merlin deficiency affects the presynaptic vesicular composition and/or organization at the climbing fiber to PC synapse. Merlin thus seems to act trans-synaptically, since Merlin expression is only altered at the postsynaptic side in PCs of L7Cre;Nf2$^{fl/fl}$ mice, but influences presynaptic parameters.

Given the alterations in dendritic branching and synapse organization of PCs in L7Cre;Nf2$^{fl/fl}$ cerebella, we analyzed mEPSCs in PCs. As shown in Fig. 6b, mEPSC amplitudes were significantly increased in knockout PCs (L7Cre;Nf2$^{fl/fl}$: 14.23 ± 0.33 pA, $n = 20$ vs. Wt;Nf2$^{fl/fl}$: 13.52 ± 0.27 pA, $n = 19$; $p < 0.001$), while the frequency was unchanged between genotypes (L7Cre;Nf2$^{fl/fl}$: 1.63 ± 0.2 Hz, $n = 20$ vs. Wt;Nf2$^{fl/fl}$: 1.65 ± 0.17 Hz, $n = 19$; $p < 0.1$).

Having shown less dendritic branching in Merlin-deficient PCs, we next analyzed axonal branching and terminal

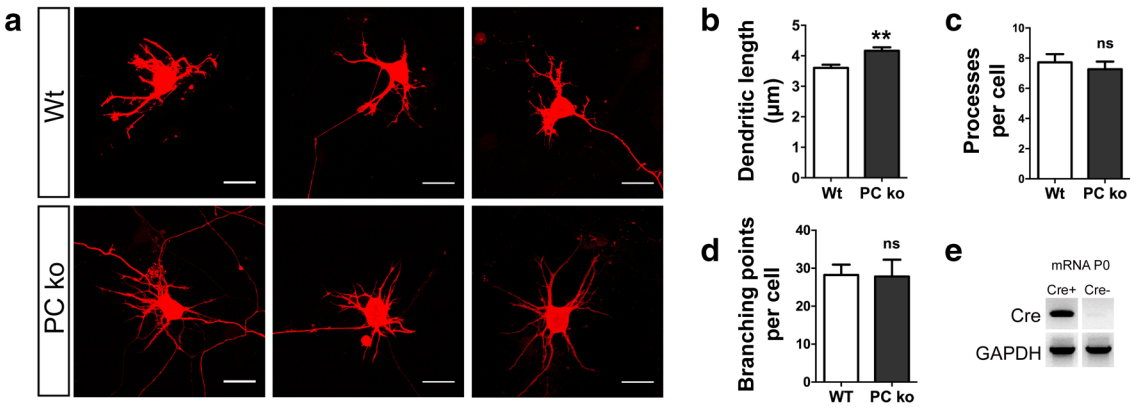

Fig. 4 Dendritic growth is increased by Merlin-specific knockout in cultured Purkinje cells. **a** Representative images of Calbindin-stained PCs cultured for 7 days in vitro. Images represent maximum intensity projections of confocal images. Scale bar: 20 µm. **b** Quantitation of dendritic length in 3D reconstructed images of L7Cre;Nf2$^{fl/fl}$ (PC ko) and Wt;Nf2$^{fl/fl}$ (Wt) PCs. Values represent mean ± SEM from three independent cultures (*$p_{\text{dendritic length}} = 0.003$, $n_{\text{Wt}} = 1300$, $n_{\text{PC ko}} = 1400$, Mann–Whitney Wilcoxon test). **c** Quantitation of numbers of processes per cell. No significant difference could be observed between Wt and PC ko mice. **d** Similarly, numbers of branch points were comparable in Wt and ko mice. **e** RT-PCR showing the expression of Cre recombinase RNA in cerebellar samples derived from newborn mice (Cre+: L7Cre;Nf2$^{fl/fl}$ transgenic mice, Cre-: Wt;Nf2$^{fl/fl}$ wild-type mice)

bouton morphology of PC axons. PC axon complexity can be shown by the number of processes within the infraganglionic plexus which can be stained by Calbindin 1 (Fig. 7a). The area covered by the stained plexus within a distance of 20 µm beneath the PC layer was comparable in both genotypes. This suggests that numbers of PC axon collaterals did not change. We then measured the size of terminal boutons around single neurons of the deep cerebellar nuclei (DCN). Terminal boutons were identified as Calbindin-positive enlargements of PC axons adjacent to the DCN. These Calbindin-positive terminals are positioned next to a gephyrin-positive postsynaptic entity. The number of larger-sized boutons was greater in the knockout than in wild-type mice. Interestingly, the number of larger-sized gephyrin dots localized postsynaptically in neurons of the DCN was also increased in Merlin-deficient PCs (Fig. 7b). In summary, we show that Merlin deficiency at the presynaptic side is important for proper sizing of presynaptic terminals. Furthermore, we can demonstrate that Merlin trans-synaptically affects the size of the postsynaptic density in DCN neurons as we demonstrated a trans-synaptic regulation of presynaptic boutons at the climbing fiber–PC synapse in Fig. 6.

Morphological consequences of Merlin deficiency in granule cells

In order to further unravel a potential function of Merlin in shaping pre- and post-synaptic structures, we used Math1Cre;Nf2$^{fl/fl}$ mice. In this mouse strain, Merlin is diminished in cerebellar granule cells, but also in afferent Mossy fibers. Math1Cre;Nf2$^{fl/fl}$ mice therefore provide synapses in which Merlin expression is only diminished at the presynaptic side (parallel fiber–PC synapse) and synapses in which Merlin expression is affected at both, pre- and postsynaptic sides (Mossy fiber–granule cell glomeruli). Before analyzing neuronal connectivity, we needed to show whether Merlin deficiency causes alterations in GC numbers. Proliferation of GC precursors takes place during the first two postnatal weeks in mice. The proliferation rate did not change as shown by the quantification of phospho-histone H3 positive neurons in the external granule cell layer (EGL) (Fig. 8a) (Hendzel et al. 1997). We also did not observe a prolongation of the proliferation phase in Math1Cre;Nf2$^{fl/fl}$ as compared to Wt;Nf2$^{fl/fl}$ mice. There was also no increase in the number of cleaved caspase-3 positive, apoptotic GCs around P8 (data not shown) which is the main time window in which GC apoptosis takes place (Wood et al. 1993). Numbers of GCs migrating radially through the molecular layer to settle within the IGL were comparable in Math1Cre;Nf2$^{fl/fl}$ and wild-type mice (IGL, Fig. 8b). In adult mice, no GC patches localized in the ML were detected, suggesting no defects on GC migration into the IGL. GC generation and overall differentiation was thus found to be normal in Merlin-deficient GCs. Therefore, there are no gross histological alterations in the cerebellum when Merlin is deleted in GCs.

In order to explore possible synaptic alterations in Math1Cre;Nf2$^{fl/fl}$ mice, we first investigated pre- and postsynaptic marker expression by Western blots of cerebellar extracts. As expected *Nf2* gene knockout by Math1-driven Cre expression led to a reduction in Merlin expression of ~ 30% compared to wild-type mice (Fig. 9a). This is a reasonable reduction given the fact, that Merlin is still expressed in all neurons and glia within the cerebellar cortex but only deleted in GCs in Math1Cre;Nf2$^{fl/fl}$ mice.

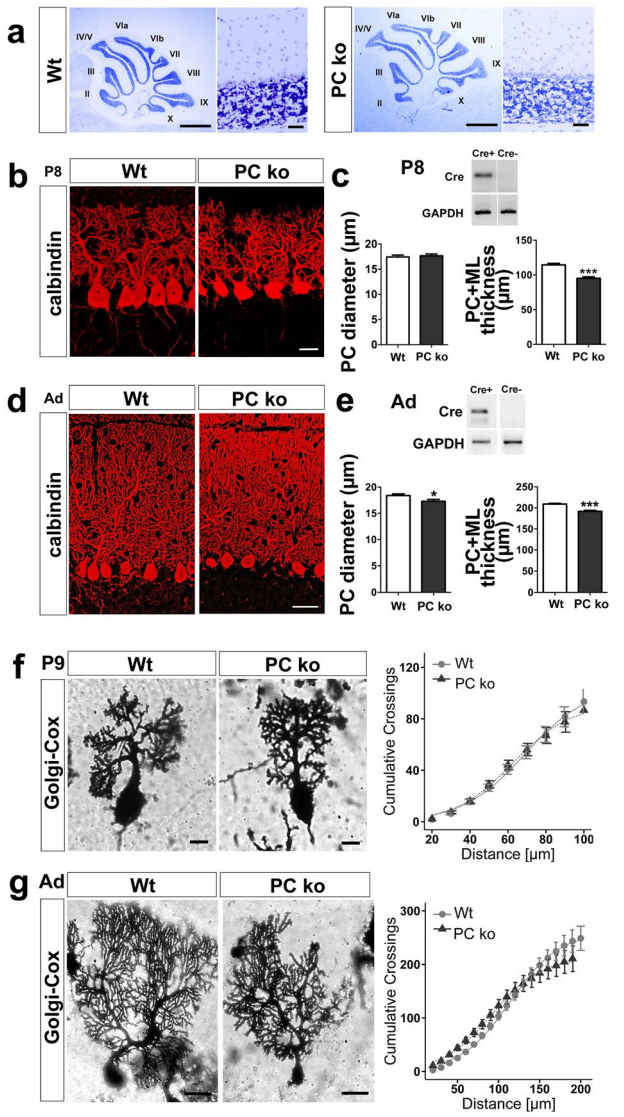

Fig. 5 NF2-deficient Purkinje cells display defects in dendritic growth and branching. **a** Sagittal vermal sections of adult cerebella derived from Wt;Nf2$^{fl/fl}$ (Wt) and L7cre;Nf2$^{fl/fl}$ (PC ko) mice were stained by cresyl violet. Higher magnifications of lobule IV reveal no alterations in lamination or layering. Scale bars: 1000 µm and 100 µm. **b** Calbindin staining of P8 cerebellar sections. Transgenic PCs form a monolayer and show normal dendritic arborization. Scale bar: 20 µm. **c** RT-PCR for Cre recombinase RNA. Cre expression could only be shown in samples from P8 cerebellum of L7Cre;Nf2$^{fl/fl}$ (Cre+) but not in those from Wt;Nf2$^{fl/fl}$ (Cre-) mice. Purkinje cell (PC) diameters and molecular layer (ML) thickness are given as mean ± SEM from three animals per genotype (***$p \leq 0.001$, $n_{PC} = 40$, $n_{sections} = 3$, Mann–Whitney Wilcoxon test). **d** Calbindin staining of adult cerebellar sections. Scale bar: 20 µm. **e** RT-PCR showing the expression of Cre recombinase RNA in samples from adult Cre+ and Cre− cerebella. PC diameters and PC and ML thickness are given as mean ± SEM from three animals per genotype (*$p_{PC\ diameter} = 0.018$, $n_{PC} = 70$; ***$p_{thickness} \leq 0.001$, $n_{regions} = 40$; Mann–Whitney Wilcoxon test). **f**, **g** Images of Golgi-stained PCs localized in lobule IV and derived from 9-day-old (P9, **f**) and adult (**g**) mice. Sholl analyses of Golgi-stained PCs are depicted as cumulative crossings of PC dendrites with circles drawn at regular distances from the soma (**f**, $p = 0.6$, $n_{Wt} = 21$, $n_{PC\ ko} = 19$; **g**, $p = 0.0012$, $n_{Wt} = 28$, $n_{PC\ ko} = 16$; Kolmogorov–Smirnov test)

Fig. 6 Purkinje cell-specific NF2 deficiency affects synaptic size and activity. **a** Western blot analysis of postsynaptic (PSD95, Homer-1) and presynaptic proteins (synaptobrevin, synaptophysin, vGluT1 and vGlut2) in adult cerebellar extracts. Synaptic marker expression was not altered in PCs of L7cre;Nf2$^{fl/fl}$ (PC ko) as compared to control (Wt) mice. Expression of pre- and post-synaptic proteins was normalized to cyclophilin setting Wt expression to 100%; the amount of phospho-Cofilin was normalized to total Cofilin levels. Results are given as mean ± SEM from three animals per genotype (*$p = 0.042$, $n = 3$; Mann–Whitney Wilcoxon test). **b** Top: mEPSC sample trace recorded from PCs of Wt and PC ko mice. Middle and bottom: cumulative distribution plots of mEPSC inter-event intervals and mEPSC amplitudes derived from Wt and PC ko mice. The knockout of Merlin in PCs resulted in increased mEPSC amplitudes as compared to Wt littermates ($p \leq 0.001$, Kolmogorov–Smirnov test), whereas the mEPSC frequency was not affected. **c** Representative confocal images of cerebellar regions from Wt and PC ko mice, double stained for Calbindin (green) and vGluT2 (red). Scale bar: 50 µm. Insets represent enlargements of a vGluT2 stained area. **d** Confocal images of cerebellar regions from Wt and ko mice, double stained for Calbindin (cyan) and vGluT1 (magenta). Scale bar: 5 µm. **e** Bar plots represent sizes and densities of vGluT2 positive puncta. Values are given as mean ± SEM from three animals per genotype (***$p = 0.0003$, $n_{puncta} > 6000$, $n_{regions} = 10$; Mann–Whitney Wilcoxon test). **f** Bar plots depict densities and lengths of dendritic spines in adult Wt and ko PCs given as mean ± SEM from three animals per genotype (*ns* not significant, $n_{Wt} > 100$, $n_{ko} > 100$, Mann–Whitney Wilcoxon test)

Levels of postsynaptic marker proteins PSD-95 and Homer were not changed (Fig. 9a) similar to our observations in cerebellar extracts derived from L7Cre;Nf2$^{fl/fl}$ mice. Analysis of presynaptic marker proteins synaptobrevin and synaptophysin also showed comparable expression levels in both genotypes. VGluT1 expression, however, was significantly increased by a factor of 2.5 suggesting that parallel fiber–PC and/or Mossy fiber–GC connectivity's were changed. Furthermore, we did see a reduction in vGluT2 expression in Math1Cre;Nf2$^{fl/fl}$ mice (Fig. 9a). These changes in vGluT expression levels prompted us to look at mEPSCs of PCs since mEPSCs are a first inroad into investigating synaptic communication in general. As opposed to L7cre;Nf2$^{fl/fl}$ mice, PCs of Math1cre;Nf2$^{fl/fl}$ mice revealed higher frequencies of mEPSCs with no change in amplitudes (Fig. 9b). Since changes in frequency are considered to be more likely caused by vesicle content in synaptic terminals or by numbers of vGluT1 terminals, we evaluated the distribution of vGluT1 staining along the PC layer to pia axis. We observed a slightly wider distribution of vGluT1 puncta reaching closer towards the PC layer in Math1cre;Nf2$^{fl/fl}$ mice as opposed to wild-type mice (Fig. 9d). Interestingly, we also observed a wider distribution of vGluT2 terminals within the molecular layer, finding more frequently vGluT2-positive puncta towards the pia of Math1cre;Nf2$^{fl/fl}$ cerebella. The size of the vGluT2 puncta was unchanged in the molecular layer raising the question why we detected a decrease in vGluT2 expression in Math1cre;Nf2$^{fl/fl}$ cerebella.

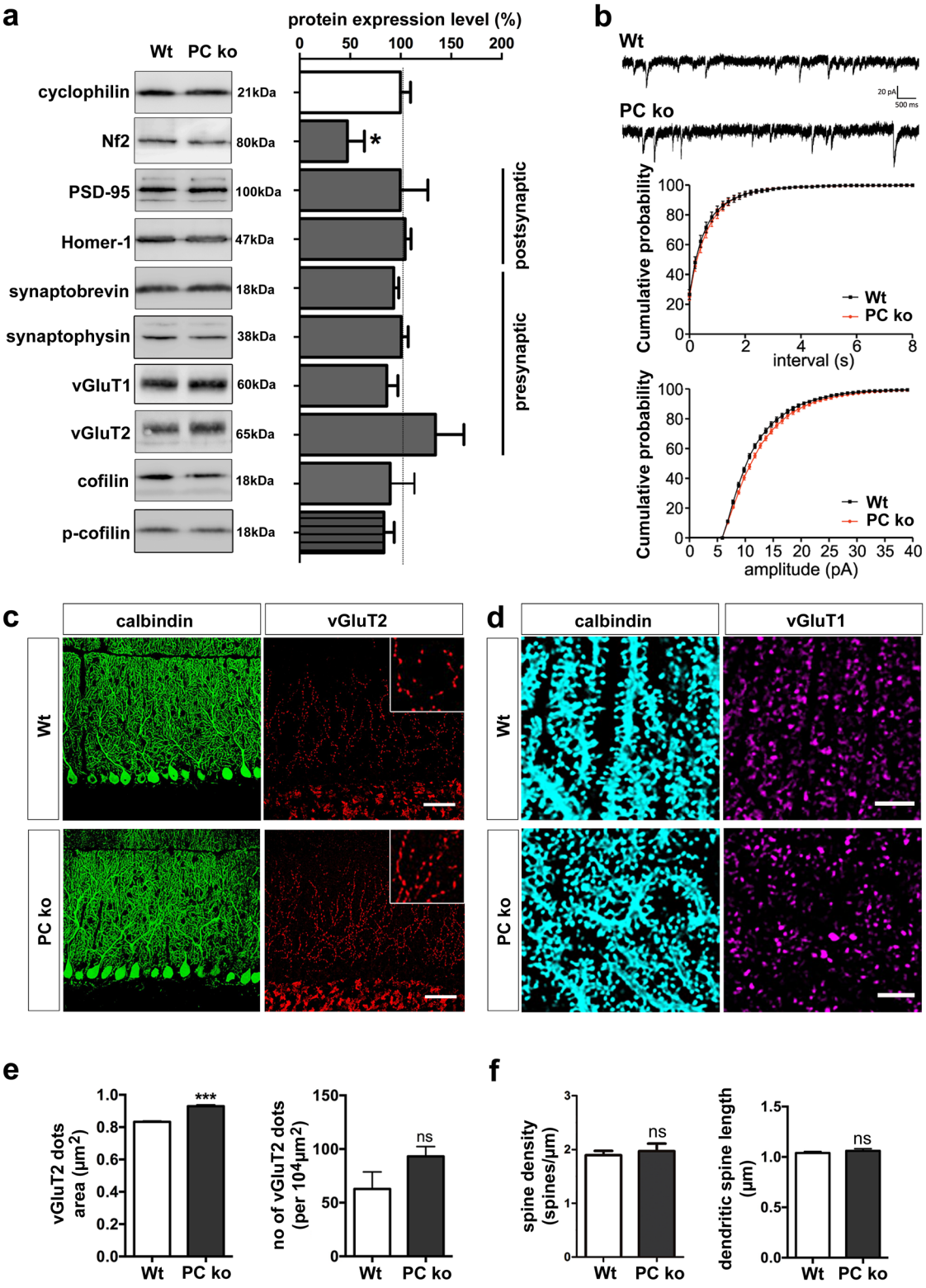

We therefore analyzed the dendritic endings of granule cells localized within the IGL. VGluT2 is present in Mossy fibers and Golgi cells both innervating granule cells. VGluT2 was prominently expressed within the IGL in both genotypes (Fig. 9c). But cluster size was significantly decreased in Math1cre;Nf2$^{fl/fl}$ cerebella as compared to wild-type mice. Clusters ranging in size between 5 and 25 µm^2—which is in the range of what was shown before (Jakab and

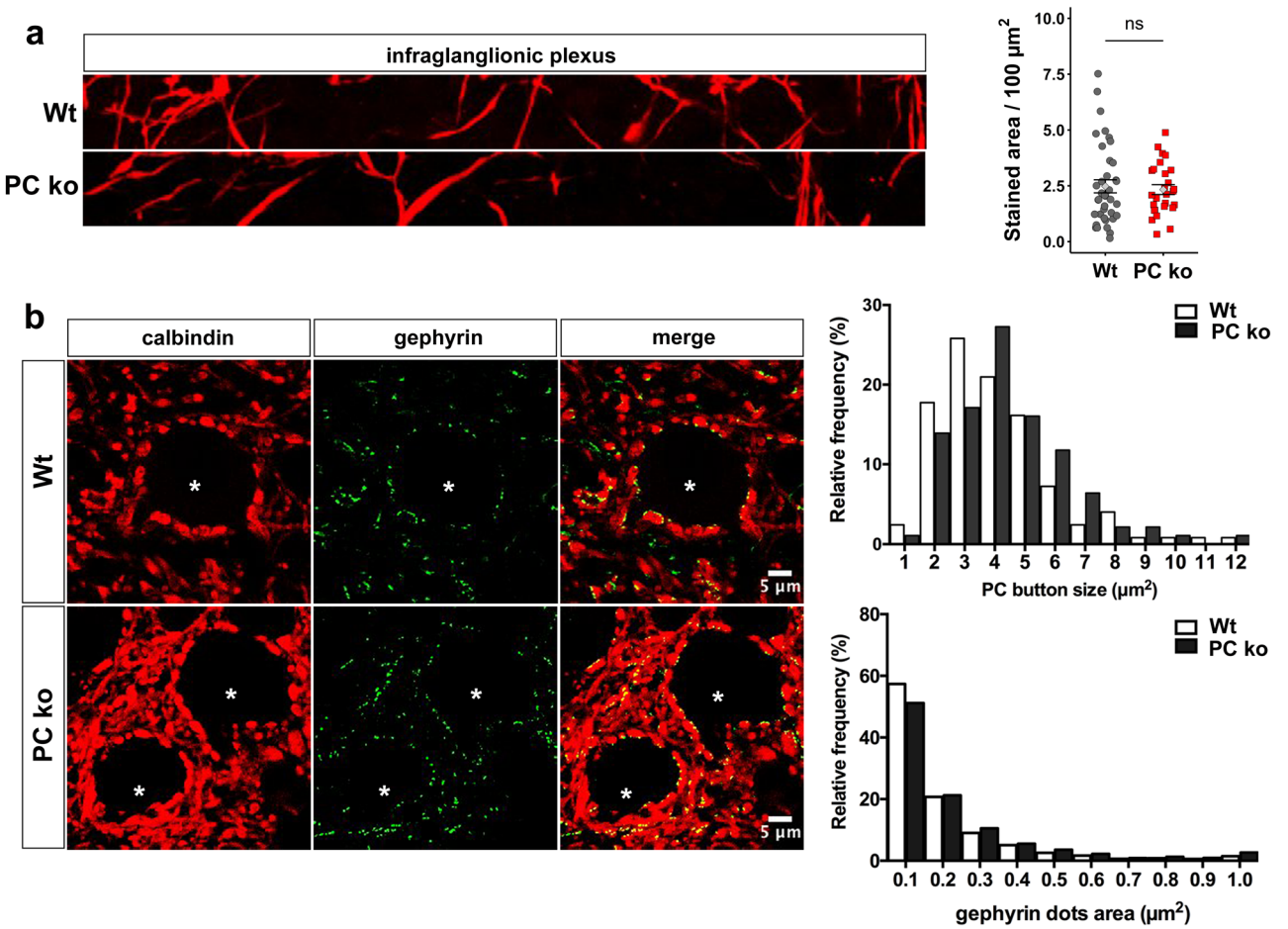

Fig. 7 Presynaptic terminals are enlarged in NF2-deficient Purkinje cells. **a** Cerebellar sagittal sections stained with Calbindin antibodies. Images display a 20-µm-thick layer beneath the PCs reaching into the granule cell layer which contains part of the infraganglionic plexus. The area covered by Calbindin-stained plexus fibers were quantitated and plotted in $\mu m^2/100\ \mu m^2$ total area. No significant difference was detected (mean ± SEM, $p = 0.7$, $n_{Wt} = 38$, $n_{PC\ ko} = 27$, one-way ANOVA). **b** Cerebellar sagittal sections immunostained for Calbindin (red) and Gephyrin (green). Deep cerebellar neurons are marked by asterisks. Scale bar: 5 µm. Nf2-deficiency in PCs increased the size of terminal buttons ($p_{button\ size} = 0.034$, $n_{Wt} = 120$, $n_{PC\ ko} = 180$, Mann–Whitney Wilcoxon test). The size of postsynaptic gephyrin dots was significantly increased ($p_{area} \leq 0.001$, $n_{Wt} = 19{,}000$, $n_{PC\ ko} = 21{,}000$, Mann–Whitney Wilcoxon test)

Hámori 1988)—were about 10% smaller in Math1Cre;$Nf2^{fl/fl}$ ($9.8 \pm 0.25\ \mu m^2$, $n = 330$) as compared to Wt;$Nf2^{fl/fl}$ mice ($10.8 \pm 0.27\ \mu m^2$, $n = 340$; $p = 0.0086$). An about 10% reduction could be observed when staining m-Cadherin clusters (39.8 ± 1.4 µm; $n_{Wt} > 800$; 36.6 ± 1.1 µm; $n_{M1\ ko} > 1000$). M-cadherin is localized in the proximity to synaptic contact sites between Mossy fibers and granule cells which might account for the larger cluster size measured (Bahjaoui-Bouhaddi et al. 1997). An about 30% reduction was found when measuring numbers of 5- to 25-μm^2-sized vGluT2 clusters within the IGL ($p_{density} = 0.008$, $n_{Wt} = 10$, $n_{M1\ ko} = 11$).

Since it has been shown that synaptogenesis is positively regulated by Rac1 signaling (Sarowar et al. 2016; Chen et al. 2010), we quantified the amount of Rac1-GTP and of phosphorylated Cofilin. The level of both proteins was increased in Math1Cre;$Nf2^{fl/fl}$ compared to wild-type mice (Fig. 9c, d) suggesting that aberrant Rac1–Cofilin signaling is involved in Merlin-mediated proper neuronal communication.

Taken together, we conclude that while Merlin deficiency in one side of a synapse causes an increase in the VGlut2 puncta, double-sided deficiency results in a decreased puncta size.

Behavioral analysis of Merlin-deficient mice

Merlin deficiency in the peripheral nervous system was shown to cause abnormal motor performance in the RotaRod test (Schulz et al. 2013a). Hence, we investigated whether synaptic alterations were associated to changes in motor learning and/or ultrasonic vocalization which both have been attributed to cerebellar dysfunctions (Tsai et al. 2012; Fujita and Momoi 2014).

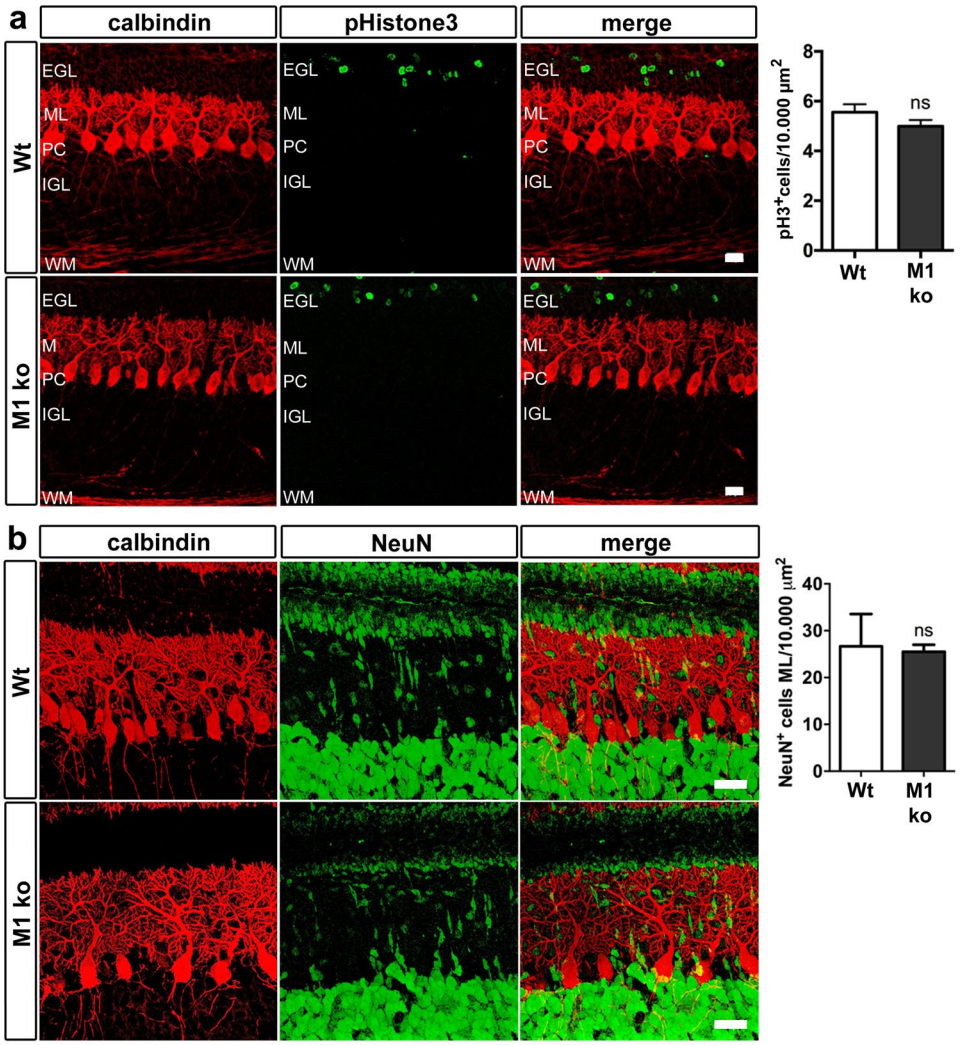

Fig. 8 Granule cell progenitor proliferation is not affected by NF2 deficiency. **a**, **b** P8 cerebellar sections immunostained for Calbindin (red) and phospho-Histone 3 (green) (**a**) or NeuN (green) (**b**). The number of proliferating phospho-Histone 3 cells was not significantly different in Math1Cre;Nf2$^{fl/fl}$ (M1 ko) and Wt;Nf2$^{fl/fl}$ (Wt) mice, nor was the number of NeuN-positive migrating granule cells in the molecular layer. Scale bar: 20 µm in **a** and **b**. *EGL* external granule cell layer, *ML* molecular layer, *PC* PC layer, *IGL* inner granule cell layer, *WM* white matter. Bar plots depict mean ± SEM. Student's *t* test were performed on data from 12 regions ($p = 0.8$)

Cerebellar function was first tested by performance of L7Cre;Nf2$^{fl/fl}$ and Math1Cre;Nf2$^{fl/fl}$ mice in a RotaRod setup. We assessed the latency to fall from a rotating stick over 5 days with four runs per day. Both conditional mice did not reveal any problems in RotaRod performance. They learned to stay on the rod equally well, and the time they stayed on the rod was comparable between transgenic and wild-type mice (Fig. 10a, b). To further explore cerebellar deficits we tested mouse pups for ultrasonic vocalizations (Bozdagi et al. 2010; Scattoni et al. 2008). Reduced ultrasonic vocalizations have been previously linked to variations in autism genes (Winslow et al. 2000; Wöhr et al. 2011; Shu et al. 2005). When comparing the average number of calls emitted by 8-day-old pups, L7Cre;Nf2$^{fl/fl}$ mice did not show a difference (Fig. 10c). Age-matched pups of Math1Cre;Nf2$^{fl/fl}$ mice, in contrast, emitted significantly less calls per minute (Fig. 10d). Consistently, the interval between calls was significantly increased in Math1Cre;Nf2$^{fl/fl}$ transgenic compared to wild-type mice, while it was unchanged in L7Cre;Nf2$^{fl/fl}$ pups (Fig. 10c, d). This change in call frequency can either be due to an overall lower calling rate, but might also be due to a developmental delay or enhanced developmental progression of cerebellar neurons in Math1Cre;Nf2$^{fl/fl}$ as compared to wild-type mice. We therefore classified the calls according to their complexity and compared frequency and duration. It turned out that the number of simple calls (short, flat, updown and chevron type) occurred significantly more often while the complex calls (complex, two syllable, multi-syllable, harmonic type) were less frequent in Math1Cre;Nf2$^{fl/fl}$ as compared to wild-type pups. In addition, although the average duration of calls was not different in both transgenic mice, the duration of the calls is highly variable between classes of calls. When we compared the average duration of calls by paired *t* tests between single classes, the duration was significantly shorter in transgenic vs. wild-type pups. This applied to both transgenic mice (Fig. 10e, f). This suggests that PC-specific knockout of Merlin caused shorter calls, and that Math1-driven Merlin deficiency caused less and shorter calls.

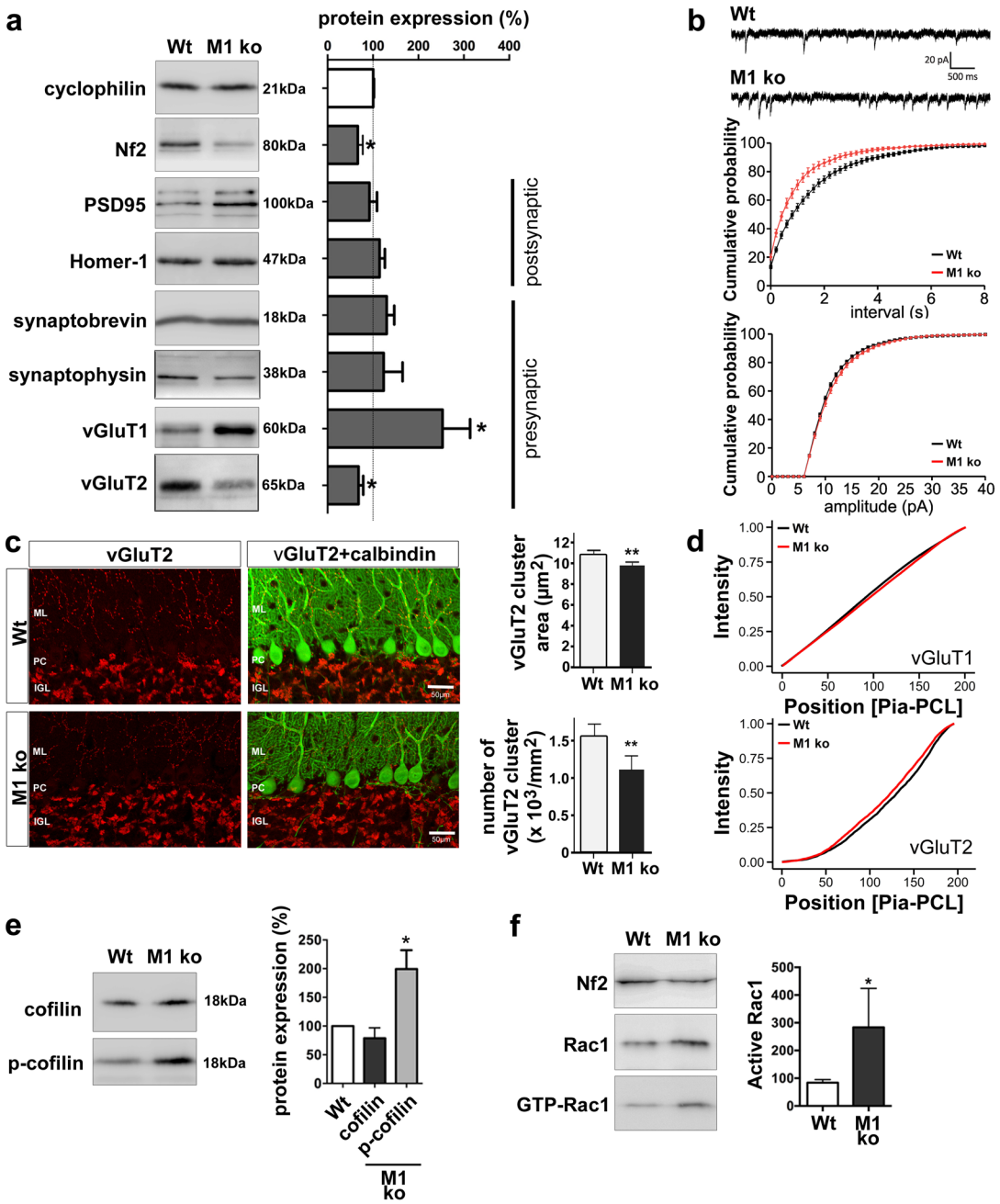

Discussion

Neurofibromatosis type 2 (NF2) is typically associated with a peripheral nervous system pathology. Expression of the *Nf2* gene product Merlin in the central nervous system and cell culture experiments, however, suggested that Merlin is also important for neuronal differentiation (Schulz et al. 2010). Using conditional knockout mice to address Merlin expression specifically in Purkinje cells (PCs) or granule cells (GCs) within the cerebellum, we provide evidence that Merlin is involved in proper dendritic growth and branching as well as correct synapse formation and function in cerebellar circuitry. The restrained effects observed likely reflect a complex mechanistic setting responsible for proper neuronal development. However, fine-tuning of synaptic contacts by Merlin in vivo, resulted in physiological and behavioral events reflecting conditions found in neurodevelopmental disorders such as autism spectrum disorders.

Axonal growth and dendritogenesis are regulated by Merlin

Using primary cell cultures derived from cell-type-specific *Nf2* knockout mice, we show here that *Nf2* deletion in GCs

◂**Fig. 9** Synaptic contact sites are affected in cerebella of Math1Cre;Nf2$^{fl/fl}$ knockout mice. **a** Western blot analysis of postsynaptic (PSD95, Homer-1) and presynaptic proteins (synaptobrevin, synaptophysin, vGluT1 and vGluT2) in adult cerebellar extracts. Expression of proteins was normalized to cyclophilin setting Wt mouse data to 100%. Relative protein levels are given as mean ± SEM from three animals per genotype (*$p_{vGluT1} = 0.016$, $p_{vGlut2} = 0.013$, $n = 3$; Mann–Whitney Wilcoxon test). **b** Top: mEPSC sample trace recorded from PCs of Wt and M1 ko mice. Middle and bottom: Cumulative distribution plots of mEPSC inter-event intervals and mEPSC amplitudes derived from Wt and M1 ko mice. The knockout of Merlin in GCs resulted in increased mEPSC frequency as compared to Wt littermates ($p \leq 0.001$, Kolmogorov–Smirnov test), whereas the mEPSC amplitude was not affected. **c** Representative confocal sections of Wt;Nf2$^{fl/fl}$ and Math1Cre;Nf2$^{fl/fl}$ cerebella stained for vGluT2 (red) and Calbindin (green). *ML* molecular layer, *PC* Purkinje cell layer, *IGL* inner granule cell layer, *WM* white matter. Scale bar: 50 µm. Bar plots depict mean ± SEM of vGluT2 positive cluster sizes and densities in the IGL. Values represent means of three animals per genotype (**$p_{puncta\ area} = 0.008$, $n_{Wt} = 344$, $n_{M1\ ko} = 330$; **$p_{puncta\ numbers} = 0.008$, $n_{Wt} = 10$, $n_{M1\ ko} = 11$; One-way ANOVA). Two areas of lobule IV were measured in three different sections per animal. **d** Cumulative distribution plots of intensity profiles derived from vGluT1 (top) and vGuT2 (bottom) stained regions spanning from the pia to the Purkinje cells layer (PCL). The vGluT1 plot of Math1Cre;Nf2$^{fl/fl}$ mice is significantly shifted to the PC layer as compared to the plot of wild-type mice ($p_{regions} < 0.0001$; $n_{Wt} = 11$, $n_{M1\ ko} = 15$, $n_{mice} = 3$, *t* test on summarized data). VGluT2 staining instead is shifted towards the pia in M1 ko mice ($p < 0.0001$; $n_{Wt} = 22$, $n_{M1\ ko} = 19$, $n_{mice} = 3$, *t* test on summarized data). **f** Western blot of adult cerebellar extracts of Wt;Nf2$^{fl/fl}$ (Wt) and Math1Cre;Nf2$^{fl/fl}$ (M1 ko) cerebella. More phosphorylated Cofilin can be detected in ko as compared to Wt cerebella. Total Cofilin amounts were quantitated and normalized against Cyclophilin loading control. Levels of phospho-Cofilin were related to the total amount of Cofilin present in the samples (*$p = 0.046$, $n = 3$, Mann–Whitney Wilcoxon test). **g** Rac1 pull down assay shows an increase in the level of GTP-Rac1 in samples from M1 ko mice indicating an increase in Rac1 activity (*$p = 0.034$, $n = 3$, Mann–Whitney Wilcoxon test)

and PCs of the cerebellum causes an increase in process outgrowth. This is consistent with a study in which Merlin overexpression and siRNA-mediated knockdown of *Nf2 mRNA* in cultured neurons repressed and increased process growth, respectively (Schulz et al. 2010). By showing an increase in process outgrowth in cultured Merlin-deficient neurons in which no other cell type is genetically modified, we demonstrated a cell-autonomous effect of Merlin. This cell-autonomous effect could be mediated by Rac1, which we found to be activated when Merlin expression was repressed in GCs. We found a significant increase in Cofilin phosphorylation, accordingly. Rac1 facilitates actin filament assembly by phosphorylating and inactivating Cofilin via p21-activated kinase (PAK) and LIM-domain containing protein kinase (LIMK) (Arber et al. 1998; Gu et al. 2010; Bamburg 1999). Rac1 stimulates spine formation, dendrite initiation, elongation, and branching complexity (Threadgill et al. 1997; Ridley 2006). Aberrant Rac1/PAK/LIMK signaling leads to abnormal neuronal connectivity and synaptic plasticity, as well as deficient cognitive and emotional behavior (Meng et al. 2004; Hayashi et al. 2004; Golden et al. 2013; Wolf et al. 2015). Rac1/Cofilin signaling therefore seems to be a plausible mediator of Merlin activity in central neurons. Considering that we found increased process growth in cultured Merlin-deficient neurons, we expected to see an increase in molecular layer thickness or dendritic segment length in L7Cre;Nf2$^{fl/fl}$ mice. Instead, we found a decrease in both parameters. In addition, PC-specific Merlin deficiency affected dendritic branching of PCs in vivo, while it did not affect the branching pattern in vitro. Although we cannot completely rule out an influence of Merlin overexpression during early stages on process formation in isoform-specific knockout mice, the same PC phenotype in isoform-specific and PC-specific knockout mice suggests that process growth is diminished in vivo by depleting Merlin.

A possible explanation for these apparent discrepancies between in vitro and in vivo data might be varying cellular environments and/or molecular interactors of Merlin. Indeed, when Merlin was expressed in neuroblastoma cells, process outgrowth did not change. However, when co-expressed together with the focal adhesion molecule paxillin, process growth was reduced (Yamauchi et al. 2008). Instead of seeing a gross morphological phenotype in conditional knockout mice, we observed changes in synaptic features. Thus, Merlin did not affect the hard-wired initial phase of PC differentiation which is characterized by a rather stereotyped way of setting up afferent innervation patterns of PCs (Coesmans et al. 2004; Hashimoto et al. 2009; Witter et al. 2016). Nonetheless, although moderately, it affected late-phase rearrangements of parallel and climbing fiber innervation (Kalinovsky et al. 2011; Ichikawa et al. 2016). In contrast to the initial phase, this second phase of remodeling and refinement of synapses requires both intrinsic as well as extrinsic factors (Sotelo and Dusart 2009). Primary dissociated cultures—in which physiological connectivity is initially disrupted and only partly restored—allowed us to unravel intrinsic versus extrinsic signaling, and suggest that Merlin's activity is influenced by the cellular environment. The molecular scenery might also be the reason for having seen different effects of Merlin deficiency on spine length and dendritic growth in isoform-specific knockout mice. Both morphological entities are filled with actin polymers, but the length, branching and style of actin bundles and the molecular regulation filament assembly and disassembly are known to differ in spines and dendrites (Georges et al. 2008; Sarowar and Grabrucker 2016; Bertling and Hotulainen 2017).

This interpretation of our results is also consistent with the notion that Merlin is not directly regulating actin polymerization and depolymerization, but instead transmits signals from the membrane (CD44, integrin, growth factors) to more downstream mediators such as Rho GTPases. Membrane-bound receptors, however, also use other

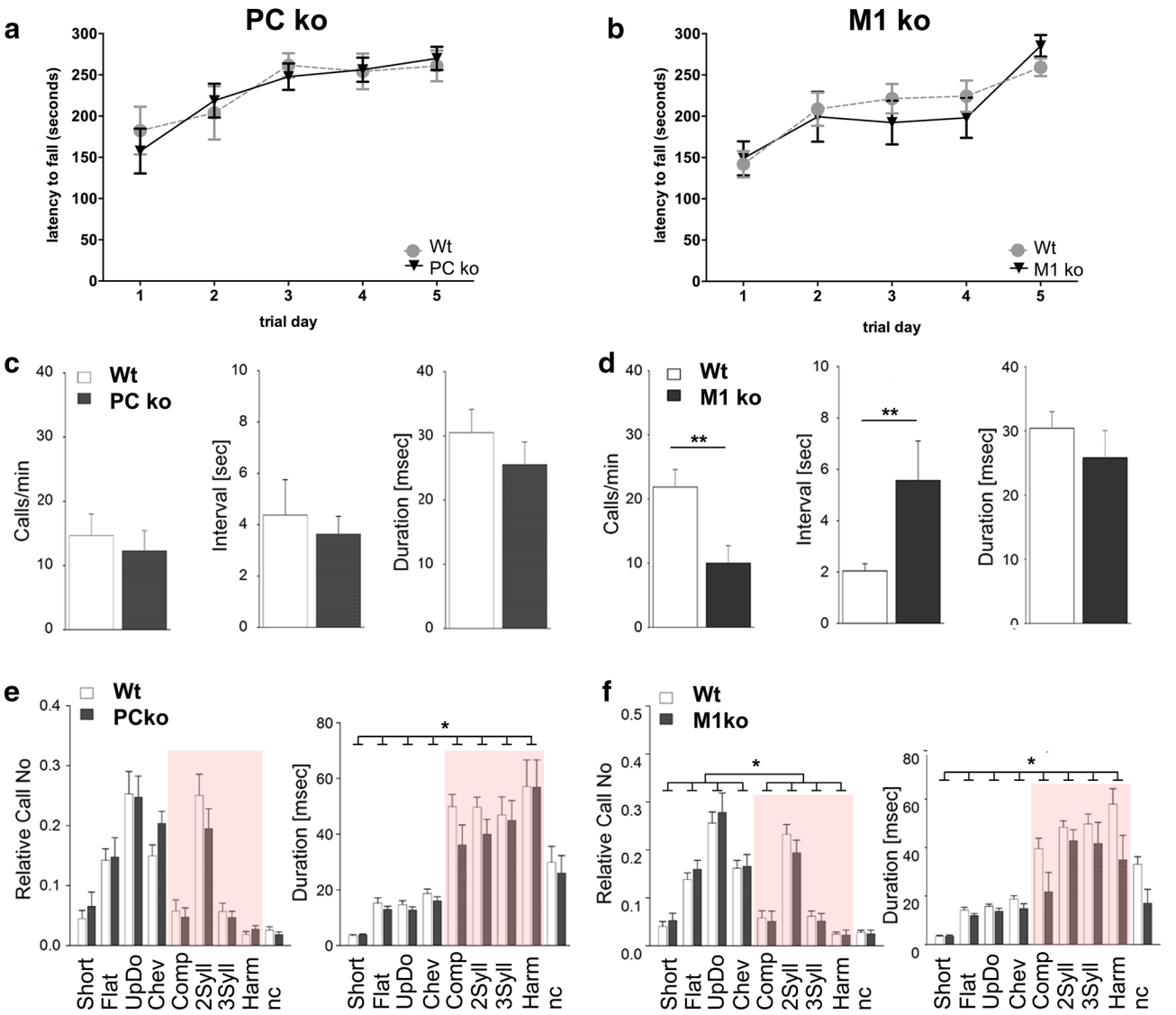

Fig. 10 Merlin knockout in Purkinje [**a**, **c**, **e**; L7Cre;Nf2$^{fl/fl}$ (L7 ko)] or granule cells [**b**, **d**, **f**; Math1Cre;Nf2$^{fl/fl}$ (M1 ko)] did not affect performance of transgenic mice on RotaRod, but changed ultrasonic vocalization. **a**, **b** Line plots depict learning curves of mice to stay on the rotating rod. No difference was observed in either genotype ($n_{Wt}=8$, $n_{L7\ ko}=7$, *t* test for time point specific data; $n_{Wt}=9$, $n_{M1\ ko}=6$, two-way ANOVA for curve comparison). **c**, **d** Bars represent mean ± SEM of total number of calls/min, of the average interval between calls and of the average duration of each call. For statistics, the means of calls of the different mice were compared, thus n is the number of mice per genotype (**$p_{calls/min}=0.0064$, $n_{Wt}=14$, $n_{L7\ ko}=13$, Mann–Whitney Wilcoxon test; $p_{interval}=0.0062$, $n_{Wt}=27$, $n_{M1\ ko}=13$, Student's *t* test). **e**, **f** Number of calls of each class related to total number of calls in each animal are plotted as mean ± SEM. The same applies for the average duration of calls for each class. The number of mice used are mentioned in **c** and **d** (**e**, *$p_{duration}=0.0140$, **f**, *$p_{duration}=0.0129$, paired Student's *t* test for comparing durations. **f** *$p_{calls/min}=0.0294$, *t* test for differences in the mean of relative call numbers)

Merlin-independent signaling pathways to alter cell morphology (e.g., Roszkowska et al. 2016; Heintz et al. 2016), which might have caused the rather mild phenotype of the conditional transgenic mice. A comparison of in vitro and in vivo data therefore allows us to postulate that Merlin deficiency intrinsically enhances neurite growth, and that these cellular responses are dependent on mechanisms implemented in the cellular environment.

Merlin expression regulates synapse formation in the cerebellum pre- and post-synaptically

Complete Merlin deficiency did not alter spine density in PCs, but seems to be necessary for proper sizing and function of synapses. When Merlin was knocked out in PCs, the amplitude of mEPSCs was increased. Alterations in mEPSC amplitudes could be caused by postsynaptic changes, i.e.,

changes in postsynaptic receptor composition, numbers of receptors at the postsynapse, channel conductivity, or the postsynaptic size. They, however, can also be caused by changes in presynaptic vesicle load. While we do not have evidence for postsynaptic changes (PSD-95 and Homer expression were unchanged), vGluT2-stained puncta and PC axonal boutons were increased in size. Since Merlin regulates microtubule-based vesicle trafficking (Hennigan et al. 2013; Jannatipour et al. 2001), Merlin might well be able to change the vesicle number within synapses and thus bouton size. There is, to our knowledge, no hint for Merlin to be able to change the vesicle load. This interpretation would be consistent with our finding that presynaptic PC terminals located around deep cerebellar neurons were enlarged. Finally, we show that vGluT1 levels present in parallel fiber terminals or presynaptic terminals of the granule cell layer were increased when Merlin was knocked out in GCs. This raises two issues: how does Merlin increase synaptic size pre- and post-synaptically, and how can it trans-synaptically regulate the presynaptic side of a synapse. Previous studies showed that members of the ADF/Cofilin family are crucial regulators of actin dynamics at the synapse. In double ADF/Cofilin knockout mice the number of synaptic vesicles clustered in the presynapse increased, leading to higher vesicle exocytosis (Wolf et al. 2015). Besides the expression level, ADF/Cofilin complex can be regulated by phosphorylation. An increase in ADF/Cofilin phosphorylation induces LTP and spine enlargement (Chen et al. 2007), while ADF/Cofilin dephosphorylation caused LTD and spine shrinkage (Zhou et al. 2004) through actin cytoskeletal remodeling. Therefore, Rac1 activation and Cofilin phosphorylation shown in Math1Cre;$Nf2^{fl/fl}$ mice may indicate that Merlin deficiency could regulate Mossy fiber–GC connections. Through a similar mechanism, the size of PC axon terminal boutons in L7Cre;$Nf2^{fl/fl}$ mice might have been affected in L7Cre;$Nf2^{fl/fl}$ mice. Unfortunately, comparable changes in Rac1/Cofilin activation/inactivation were not detected, probably due to the rather small PCs protein content in total cerebellar extracts. Merlin was also shown to be important for receptor internalization. When blocking Merlin expression in colonic epithelial cells, the amount of vesicles was highly increased and membrane borders have been greatly enlarged (Chiasson-MacKenzie et al. 2015). Again, Rac1/Cofilin/actin signaling is a plausible mediator of membrane trafficking at the synapse. Cofilin was found to be present in dendrites, dendritic spines and postsynaptic densities (Racz and Weinberg 2006; Liu et al. 2016). Thus, Merlin could cause an imbalance of exocytosis and endocytosis at the synapse leading to presynaptic vesicle accumulation.

While it is possible that Merlin intrinsically affects cell morphology given its function as a cytoskeleton-associated molecule, it was surprising to see a trans-synaptic effect of Merlin deficiency as the increase in size of the vGluT2-positive puncta in the molecular layer of L7Cre;$Nf2^{fl/fl}$ mice. A similar postulate has been proposed for Merlin in neuron–glia interaction in the peripheral nervous system. When Merlin was specifically diminished in peripheral neurons, myelin sheaths adapted by a Neuregulin/ERBB2-dependent mechanism (Schulz et al. 2013b). Neuregulin/ERBB signaling is also required at the synaptic junction where it modulates both the pre- and post-synaptic terminals. When ERBB4 is activated in cerebral inhibitory neurons, dendritic and synaptic growth is increased (Unda et al. 2016). A large body of evidence suggests that trans-synaptic interactions between synaptic adhesion molecules function bi-directionally for synapse formation and maturation. Therefore, the enlargement of the presynapse might lead to the presence of more adhesion molecules in the membrane which are contacted in turn by an enlarged postsynapse (Scheiffele et al. 2000; Graf et al. 2004; Chih et al. 2005; Nam and Chen 2005; Chubykin et al. 2007). The increase in postsynaptic (gephyrin positive) terminal size might therefore be explained by a compensatory effect mediated by synaptic adhesion molecules. Provided that post- and pre-synaptic signaling are affected by Merlin deficiency, and since both sides of the synapse might be affected differentially by its expression, Merlin deficiency on one side might produce a phenomenon different to missing Merlin on both sides of the synapse. Indeed, we found that eliminating one Merlin isoform (either 1 or 2) on both sides of the synapse, produced a diminished synaptic size, while it was enlarged when only one side was affected.

Morphological alterations found in the cell-type-specific knockout mice are supported by the electrophysiological experiments which show a reduction in spontaneous synaptic activity. They are also supported by our ultrasonic vocalization data demonstrating a decrease in the duration of simple calls and, in the case of the GC-specific Merlin-deficient mice, changes in number of vocals. Although this is not solely attributable to the cerebellum, it has to be noted that the cerebellum is not only involved in motor learning, but seems to be crucial for non-motor tasks related to emotional, cognitive and social events (Shevelkin et al. 2014). This new view of cerebellar function could also explain why we did not see alterations in motor behavior, which are mainly seen after gross morphological alterations of the cerebellar cortex. The behavioral studies support a function of Merlin in fine-tuning of neuronal synapses within the central nervous system potentially impacting on synaptic communication.

Acknowledgements This work was supported by the Alexander von Humboldt foundation (HERMES to A.T.) and BONFOR grant O-167.0017 (to S.L.B.). The authors are very grateful to Stefanie Ramrath and Sabine Molly-Klumbies for excellent technical help, and Daniela Krauss and Narziss Haias for provident animal husbandry. We

would like to acknowledge Dr. Daniel Prieto for thorough comments during the preparation of this manuscript.

Compliance with ethical standards

Conflict of interest The authors declare that they have no conflict of interest, neither commercial nor non-commercial. All applicable international, national, and/or institutional guidelines for the care and use of animals were followed (see "Materials and methods" section for details). This article does not contain any studies with human participants performed by any of the authors.

References

Arber S, Barbayannis FA, Hanser H, Schneider C, Stanyon CA, Bernard O, Caroni P (1998) Regulation of actin dynamics through phosphorylation of cofilin by LIM-kinase. Nature 393:805–809

Avery AW, Thomas DD, Hays TS (2017) β-III-spectrin spinocerebellar ataxia type 5 mutation reveals a dominant cytoskeletal mechanism that underlies dendritic arborization. Proc Natl Acad Sci USA 114:E9376–E9385

Baader SL, Schilling K (1996) Glutamate receptors mediate dynamic regulation of nitric oxide synthase expression in cerebellar granule cells. J Neurosci 16:1440–1449

Bahjaoui-Bouhaddi M, Padilla F, Nicolet M, Cifuentes-Diaz C, Fellmann D, Mege RM (1997) Localized deposition of m-cadherin in the glomeruli of the granular layer during the postnatal development of mouse cerebellum. J Comp Neurol 378:180–195

Bamburg JR (1999) Proteins of the ADF/cofilin family: essential regulators of actin dynamics. Annu Rev Cell Dev Biol 15:185–230

Baptista CA, Hatten ME, Blazeski R, Mason CA (1994) Cell-cell interactions influence survival and differentiation of purified Purkinje cells in vitro. Neuron 12:243–260

Barski JJ, Dethleffsen K, Meyer M (2000) Cre recombinase expression in cerebellar Purkinje cells. Genesis 28:93–98

Bertling E, Hotulainen P (2017) New waves in dendritic spine actin cytoskeleton. From branches and bundles to rings, from actin binding proteins to post-translational modifications. Mol Cell Neurosci 84:77–84

Borovac J, Bosch M, Okamoto K (2018) Regulation of actin dynamics during structural plasticity of dendritic spines. Signaling messengers and actin-binding proteins. Mol Cell Neurosci 91:122–130

Bozdagi O, Sakurai T, Papapetrou D, Wang X, Dickstein DL, Takahashi N, Kajiwara Y, Yang M, Katz AM, Scattoni ML, Harris MJ, Saxena R, Silverman JL, Crawley JN, Zhou Q, Hof PR, Buxbaum JD (2010) Haploinsufficiency of the autism-associated Shank3 gene leads to deficits in synaptic function, social interaction, and social communication. Mol Autism 1:15

Chen LY, Rex CS, Casale MS, Gall CM, Lynch G (2007) Changes in synaptic morphology accompany actin signaling during LTP. J Neurosci 27:5363–5372

Chen LY, Rex CS, Babayan AH, Kramar EA, Lynch G, Gall CM, Lauterborn JC (2010) Physiological activation of synaptic Rac-PAK (p-21 activated kinase) signaling is defective in a mouse model of fragile X syndrome. J Neurosci 30:10977–10984

Chiasson-MacKenzie C, Morris ZS, Baca Q, Morris B, Coker JK, Mirchev R, Jensen AE, Carey T, Stott SL, Golan DE, McClatchey AI (2015) NF2/Merlin mediates contact-dependent inhibition of EGFR mobility and internalization via cortical actomyosin. J Cell Biol 211:391–405

Chih B, Engelman H, Scheiffele P (2005) Control of excitatory and inhibitory synapse formation by neuroligins. Science 307:1324–1328

Chubykin AA, Atasoy D, Etherton MR, Brose N, Kavalali ET, Gibson JR, Sudhof TC (2007) Activity-dependent validation of excitatory versus inhibitory synapses by neuroligin-1 versus neuroligin-2. Neuron 54:919–931

Coesmans M, Weber JT, de Zeeuw CI, Hansel C (2004) Bidirectional parallel fiber plasticity in the cerebellum under climbing fiber control. Neuron 44:691–700

den Bakker MA, Vissers KJ, Molijn AC, Kros JM, Zwarthoff EC, van der Kwast TH (1999) Expression of the neurofibromatosis type 2 gene in human tissues. J Histochem Cytochem 47:1471–1480

Development Core Team R (2008) R: a language and environment for statistical computing. R Foundation for Statistical Computing, Vienna

Ferner RE (2007) Neurofibromatosis 1 and neurofibromatosis 2: a twenty first century perspective. Lancet Neurol 6:340–351

Ferreira TA, Blackman AV, Oyrer J, Jayabal S, Chung AJ, Watt AJ, Sjostrom PJ, van Meyel DJ (2014) Neuronal morphometry directly from bitmap images. Nat Meth 11:982–984

Fujita E, Momoi T (2014) Specific expression of FOXP2 in cerebellum improves ultrasonic vocalization in heterozygous but not in homozygous Foxp2 (R552H) knock-in pups. Neurosci Lett 566:162–166

Georges PC, Hadzimichalis NM, Sweet ES, Firestein BL (2008) The yin–yang of dendrite morphology: unity of actin and microtubules. Mol Neurobiol 38:270–284

Gliem M, Weisheit G, Mertz KD, Endl E, Oberdick J, Schilling K (2006) Expression of classical cadherins in the cerebellar anlage: quantitative and functional aspects. Mol Cell Neurosci 33:447–458

Golden SA, Christoffel DJ, Heshmati M, Hodes GE, Magida J, Davis K, Cahill ME, Dias C, Ribeiro E, Ables JL, Kennedy PJ, Robison AJ, Gonzalez-Maeso J, Neve RL, Turecki G, Ghose S, Tamminga CA, Russo SJ (2013) Epigenetic regulation of RAC1 induces synaptic remodeling in stress disorders and depression. Nat Med 19:337–344

Graf ER, Zhang X, Jin SX, Linhoff MW, Craig AM (2004) Neurexins induce differentiation of GABA and glutamate postsynaptic specializations via neuroligins. Cell 119:1013–1026

Gu J, Lee CW, Fan Y, Komlos D, Tang X, Sun C, Yu K, Hartzell HC, Chen G, Bamburg JR, Zheng JQ (2010) ADF/cofilin-mediated actin dynamics regulate AMPA receptor trafficking during synaptic plasticity. Nat Neurosci 13:1208–1215

Gutmann DH, Wright DE, Geist RT, Snider WD (1995) Expression of the neurofibromatosis 2 (NF2) gene isoforms during rat embryonic development. Hum. Mol. Genet. 4:471–478

Hansen ST, Meera P, Otis TS, Pulst SM (2012) Changes in Purkinje cell firing and gene expression precede behavioral pathology in a mouse model of SCA2. Hum Mol Genet 22:271–283

Hashimoto K, Ichikawa R, Kitamura K, Watanabe M, Kano M (2009) Translocation of a "Winner" climbing fiber to the Purkinje cell dendrite and subsequent elimination of "Losers" from the soma in developing cerebellum. Neuron 63:106–118

Hayashi ML, Choi S-Y, Rao BSS, Jung H-Y, Lee H-K, Zhang D, Chattarji S, Kirkwood A, Tonegawa S (2004) Altered cortical synaptic morphology and impaired memory consolidation in forebrain- specific dominant-negative PAK transgenic mice. Neuron 42:773–787

Heintz TG, Eva R, Fawcett JW (2016) Regional regulation of Purkinje cell dendritic spines by integrins and Eph/Ephrins. PLoS One 11:e0158558

Hendzel MJ, Wei Y, Mancini MA, van Hooser A, Ranalli T, Brinkley BR, Bazett-Jones DP, Allis CD (1997) Mitosis-specific phosphorylation of histone H3 initiates primarily within pericentromeric heterochromatin during G2 and spreads in an ordered fashion coincident with mitotic chromosome condensation. Chromosoma 106:348–360

Hennigan RF, Moon CA, Parysek LM, Monk KR, Morfini G, Berth S, Brady S, Ratner N (2013) The NF2 tumor suppressor regulates microtubule-based vesicle trafficking via a novel Rac, MLK and p38(SAPK) pathway. Oncogene 32:1135–1143

Hioki H, Fujiyama F, Taki K, Tomioka R, Furuta T, Tamamaki N, Kaneko T (2003) Differential distribution of vesicular glutamate transporters in the rat cerebellar cortex. Neuroscience 117:1–6

Holst MI, Maercker C, Pintea B, Masseroli M, Liebig C, Jankowski J, Miething A, Martini J, Schwaller B, Oberdick J, Schilling K, Baader SL (2008) Engrailed-2 regulates genes related to vesicle formation and transport in cerebellar Purkinje cells. Mol Cell Neurosci 38:495–504

Huynh DP, Tran TM, Nechiporuk T, Pulst SM (1996) Expression of neurofibromatosis 2 transcript and gene product during mouse fetal development. Cell Growth Differ 7:1551–1561

Ichikawa R, Hashimoto K, Miyazaki T, Uchigashima M, Yamasaki M, Aiba A, Kano M, Watanabe M (2016) Territories of heterologous inputs onto Purkinje cell dendrites are segregated by mGluR1-dependent parallel fiber synapse elimination. Proc Natl Acad Sci USA 113:2282–2287

Ito M (2002) The molecular organization of cerebellar long-term depression. Nat Rev Neurosci 3:896–902

Jakab RL, Hámori J (1988) Quantitative morphology and synaptology of cerebellar glomeruli in the rat. Anat Embryol 179:81–88

Jankowski J, Holst MI, Liebig C, Oberdick J, Baader SL (2004) Engrailed-2 negatively regulates the onset of perinatal Purkinje cell differentiation. J Comp Neurol 472:87–99

Jannatipour M, Dion P, Khan S, Jindal H, Fan X, Laganiere J, Chishti AH, Rouleau GA (2001) Schwannomin isoform-1 interacts with syntenin via PDZ domains. J Biol Chem 276:33093–33100

Kalinovsky A, Boukhtouche F, Blazeski R, Bornmann C, Suzuki N, Mason CA, Scheiffele P (2011) Development of axon-target specificity of ponto-cerebellar afferents. PLoS Biol 9:e1001013

Kissil JL, Johnson KC, Eckman MS, Jacks T (2002) Merlin phosphorylation by p21-activated kinase 2 and effects of phosphorylation on merlin localization. J Biol Chem 277:10394–10399

Kuhn TB, Meberg PJ, Brown MD, Bernstein BW, Minamide LS, Jensen JR, Okada K, Soda EA, Bamburg JR (2000) Regulating actin dynamics in neuronal growth cones by ADF/cofilin and Rho family GTPases. J Neurobiol 44:126–144

Li W, Cooper J, Karajannis MA, Giancotti FG (2012) Merlin: a tumour suppressor with functions at the cell cortex and in the nucleus. EMBO Rep 13(3):204–215

Liu A, Zhou Z, Dang R, Zhu Y, Qi J, He G, Leung C, Pak D, Jia Z, Xie W (2016) Neuroligin 1 regulates spines and synaptic plasticity via LIMK1/cofilin-mediated actin reorganization. J Cell Biol 212:449–463

Matei V, Pauley S, Kaing S, Rowitch D, Beisel KW, Morris K, Feng F, Jones K, Lee J, Fritzsch B (2005) Smaller inner ear sensory epithelia in Neurog 1 null mice are related to earlier hair cell cycle exit. Dev Dyn 234:633–650

McClatchey AI, Fehon RG (2009) Merlin and the ERM proteins–regulators of receptor distribution and signaling at the cell cortex. Trends Cell Biol. 19:198–206

McClatchey AI, Saotome I, Ramesh V, Gusella JF, Jacks T (1997) The Nf2 tumor suppressor gene product is essential for extraembryonic development immediately prior to gastrulation. Genes Dev 11:1253–1265

Meng Y, Takahashi H, Meng J, Zhang Y, Lu G, Asrar S, Nakamura T, Jia Z (2004) Regulation of ADF/cofilin phosphorylation and synaptic function by LIM-kinase. Neuropharmacology 47:746–754

Morrison H, Sperka T, Manent J, Giovannini M, Ponta H, Herrlich P (2007) Merlin/neurofibromatosis type 2 suppresses growth by inhibiting the activation of Ras and Rac. Cancer Res 67:520–527

Muller W, Connor JA (1991) Dendritic spines as individual neuronal compartments for synaptic Ca^{2+} responses. Nature 354:73–76

Nam CI, Chen L (2005) Postsynaptic assembly induced by neurexin-neuroligin interaction and neurotransmitter. Proc Natl Acad Sci USA 102:6137–6142

Ng J, Luo L (2004) Rho GTPases regulate axon growth through convergent and divergent signaling pathways. Neuron 44:779–793

Palay SL, Chan-Palay V (1974) Cerebellar cortex. Cytology and organization. Springer, New York

Pan N, Jahan I, Lee JE, Fritzsch B (2009) Defects in the cerebella of conditional Neurod1 null mice correlate with effective Tg(Atoh1-cre) recombination and granule cell requirements for Neurod1 for differentiation. Cell Tissue Res 337:407–428

Pfaffl MW (2001) A new mathematical model for relative quantification in real-time RT-PCR. Nucleic Acids Res 29:e45

Powell SK, Rivas RJ, Rodriguez-Boulan E, Hatten ME (1997) Development of polarity in cerebellar granule cells. J Neurobiol 32:223–236

Racz B, Weinberg RJ (2006) Spatial organization of cofilin in dendritic spines. Neuroscience 138:447–456

Ramesh V (2004) Merlin and the ERM proteins in Schwann cells, neurons and growth cones. Nat Rev Neurosci 5:462–470

Ridley AJ (2006) Rho GTPases and actin dynamics in membrane protrusions and vesicle trafficking. Trends Cell Biol 16:522–529

Roszkowska M, Skupien A, Wojtowicz T, Konopka A, Gorlewicz A, Kisiel M, Bekisz M, Ruszczycki B, Dolezyczek H, Rejmak E, Knapska E, Mozrzymas JW, Wlodarczyk J, Wilczynski GM, Dzwonek J (2016) CD44: a novel synaptic cell adhesion molecule regulating structural and functional plasticity of dendritic spines. Mol Biol Cell 27:4055–4066

Sarowar T, Grabrucker AM (2016) Actin-dependent alterations of dendritic spine morphology in shankopathies. Neural Plast 2016:8051861

Sarowar T, Grabrucker S, Föhr K, Mangus K, Eckert M, Bockmann J, Boeckers TM, Grabrucker AM (2016) Enlarged dendritic spines and pronounced neophobia in mice lacking the PSD protein RICH2. Mol Brain 9:409

Sassoe-Pognetto M, Patrizi A (2017) The Purkinje cell as a model of synaptogenesis and synaptic specificity. Brain Res Bull 129:12–17

Scattoni ML, Gandhy SU, Ricceri L, Crawley JN (2008) Unusual repertoire of vocalizations in the BTBR T + tf/J mouse model of Autism. PLoS One 3:e3067–e3081

Scheiffele P, Fan J, Choih J, Fetter R, Serafini T (2000) Neuroligin expressed in nonneuronal cells triggers presynaptic development in contacting axons. Cell 101:657–669

Schilling K, Dickinson MH, Connor JA, Morgan JI (1991) Electrical activity in cerebellar cultures determines Purkinje cell dendritic growth patterns. Neuron 7:891–902

Schindelin J, Arganda-Carreras I, Frise E, Kaynig V, Longair M, Pietzsch T, Preibisch S, Rueden C, Saalfeld S, Schmid B, Tinevez J-Y, White DJ, Hartenstein V, Eliceiri K, Tomancak P, Cardona A (2012) Fiji: an open-source platform for biological-image analysis. Nat Meth 9:676–682

Schulz A, Geissler KJ, Kumar S, Leichsenring G, Morrison H, Baader SL (2010) Merlin inhibits neurite outgrowth in the CNS. J Neurosci 30:10177–10186

Schulz A, Baader SL, Niwa-Kawakita M, Jung MJ, Bauer R, Garcia CA, Zoch A, Schacke S, Hagel C, Mautner VF, Hanemann CO, Dun XP, Parkinson DB, Weis J, Schroder JM, Gutmann DH, Giovannini M, Morrison H (2013a) Merlin isoform 2 in neurofibromatosis type 2-associated polyneuropathy. Nat Neurosci 16:426–433

Schulz A, Kyselyova A, Baader SL, Jung MJ, Zoch A, Mautner VF, Hagel C, Morrison H (2013b) Neuronal merlin influences ERBB2 receptor expression on Schwann cells through neuregulin 1 type III signalling. Brain 137:420–432

Shaw RJ, Paez JG, Curto M, Yaktine A, Pruitt WM, Saotome I, O'Bryan JP, Gupta V, Ratner N, Der CJ, Jacks T, McClatchey

AI (2001) The Nf2 tumor suppressor, merlin, functions in Rac-dependent signaling. Dev Cell 1:63–72
Sher I, Hanemann CO, Karplus PA, Bretscher A (2012) The tumor suppressor merlin controls growth in its open state, and phosphorylation converts it to a less-active more-closed state. Dev Cell 22:703–705
Shevelkin AV, Ihenatu C, Pletnikov MV (2014) Pre-clinical models of neurodevelopmental disorders: focus on the cerebellum. Rev Neurosci 25:177–194
Sholl DA (1953) Dendritic organization in the neurons of the visual and motor cortices of the cat. J Anat 87:387–406
Shu W, Cho JY, Jiang Y, Zhang M, Weisz D, Elder GA, Schmeidler J, de Gasperi R, Sosa MAG, Rabidou D, Santucci AC, Perl D, Morrisey E, Buxbaum JD (2005) Altered ultrasonic vocalization in mice with a disruption in the Foxp2 gene. Proc Natl Acad Sci USA 102:9643–9648
Sotelo C, Dusart I (2009) Intrinsic versus extrinsic determinants during the development of Purkinje cell dendrites. Neuroscience 162:589–600
Surace EI, Haipek CA, Gutmann DH (2004) Effect of merlin phosphorylation on neurofibromatosis 2 (NF2) gene function. Oncogene 23:580–587
Threadgill R, Bobb K, Ghosh A (1997) Regulation of dendritic growth and remodeling by Rho, Rac, and Cdc42. Neuron 19:625–634
Tsai PT, Hull C, Chu Y, Greene-Colozzi E, Sadowski AR, Leech JM, Steinberg J, Crawley JN, Regehr WG, Sahin M (2012) Autistic-like behaviour and cerebellar dysfunction in Purkinje cell Tsc1 mutant mice. Nature 488:647–651
Unda BK, Kwan V, Singh KK (2016) Neuregulin-1 regulates cortical inhibitory neuron dendrite and synapse growth through DISC1. Neural Plast 2016:7694385
Voogd J, Glickstein M (1998) The anatomy of the cerebellum. Trends Neurosci 21:370–375
White JJ, Arancillo M, Stay TL, George-Jones NA, Levy SL, Heck DH, Sillitoe RV (2014) Cerebellar zonal patterning relies on Purkinje cell neurotransmission. J Neurosci 34:8231–8245
Winslow JT, Hearn EF, Ferguson J, Young LJ, Matzuk MM, Insel TR (2000) Infant vocalization, adult aggression, and fear behavior of an oxytocin null mutant mouse. Horm Behav 37:145–155
Witter L, Rudolph S, Pressler RT, Lahlaf SI, Regehr WG (2016) Purkinje cell collaterals enable output signals from the cerebellar cortex to feed back to purkinje cells and interneurons. Neuron 91:312–319
Wöhr M, Roullet FI, Hung AY, Sheng M, Crawley JN (2011) Communication impairments in mice lacking Shank1. Reduced levels of ultrasonic vocalizations and scent marking behavior. PLoS One 6:e20631
Wolf M, Zimmermann A-M, Görlich A, Gurniak CB, Sassoè-Pognetto M, Friauf E, Witke W, Rust MB (2015) ADF/Cofilin controls synaptic actin dynamics and regulates synaptic vesicle mobilization and exocytosis. Cereb Cortex 25:2863–2875
Wood KA, Dipasquale B, Youle RJ (1993) Insitu labeling of granule cells for apoptosis-associated DNA fragmentation reveals different mechanisms of cell loss in developing cerebellum. Neuron 11:621–632
Xing W, Li M, Zhang F, Ma X, Long J, Zhou H (2017) The conformation change and tumor suppressor role of Merlin are both independent of Serine 518 phosphorylation. Biochem Biophys Res Commun 493:46–51
Yamauchi J, Miyamoto Y, Kusakawa S, Torii T, Mizutani R, Sanbe A, Nakajima H, Kiyokawa N, Tanoue A (2008) Neurofibromatosis 2 tumor suppressor, the gene induced by valproic acid, mediates neurite outgrowth through interaction with paxillin. Exp Cell Res 314:2279–2288
Zhou Q, Homma KJ, Poo MM (2004) Shrinkage of dendritic spines associated with long-term depression of hippocampal synapses. Neuron 44:749–757
Zoch A, Mayerl S, Schulz A, Greither T, Frappart L, Rubsam J, Heuer H, Giovannini M, Morrison H (2015) Merlin isoforms 1 and 2 both act as tumour suppressors and are required for optimal sperm maturation. PLoS One 10:e0129151